Nanoscale Horizons

REVIEW

View Article Online
View Journal | View Issue

Cite this: *Nanoscale Horiz.*, 2019, 4, 809

Theory-guided materials design: two-dimensional MXenes in electro- and photocatalysis

Albertus D. Handoko, [a] Stephan N. Steinmann [b] and Zhi Wei Seh *[a]

Received 20th February 2019,
Accepted 3rd April 2019

DOI: 10.1039/c9nh00100j

rsc.li/nanoscale-horizons

Two-dimensional transition metal carbides and nitrides (MXenes) have made a significant impact on sustainable energy research in the fields of energy storage and conversion. Unlike short-term energy storage strategies (*e.g.* batteries and supercapacitors), catalytic conversion of simple molecules to value-added chemicals using renewable energy represents a more long-term solution to the world's energy crisis. Significant advances in density functional theory and low-cost computing in the past decade have enabled the generation of reliable materials data from fundamental physics equations. The paradigm shift towards theory-guided materials design is expected to enhance the catalyst discovery and development process by providing rational guidance to screen viable MXene catalysts more rapidly than an experimental-only approach. In this review, we aim to provide a critical appraisal of the latest theoretical and experimental work on MXenes in the fields of electro- and photocatalytic energy conversion, including relevant reactions involving hydrogen, oxygen, carbon dioxide and nitrogen molecules. In the process, we will also be pointing out current limitations in theoretical models, existing scientific gaps and future research directions for this field.

1. Introduction

The burgeoning energy demand linked to rapid global population growth and expanding industrialization calls for new sources of sustainable and renewable energy. The U.S. Energy Information Administration estimates that close to 80% of the world's primary energy consumption is derived from fossil fuels, including coal, natural gas, petroleum, and related products.[1] Fossil fuel is not a

[a] *Institute of Materials Research and Engineering, Agency for Science, Technology and Research (A*STAR), 2 Fusionopolis Way, Innovis, Singapore 138634, Singapore. E-mail: sehzw@imre.a-star.edu.sg*
[b] *Univ Lyon, ENS de Lyon, CNRS, Université Lyon 1, Laboratoire de Chimie UMR 5182, F-69342, Lyon, France*

Albertus D. Handoko

*Albertus Denny Handoko is a Scientist at the Institute of Materials Research and Engineering, A*STAR. He attained his core competency in solvothermal/hydrothermal synthesis methods and X-ray characterisation during his PhD studies at Nanyang Technological University (Singapore). He went for postdoctoral research fellowships at the University College London (UK) and National University of Singapore where he gained research experience and developed keen interest in photo- and electrochemistry. His current research effort is dedicated to understanding advanced electrocatalytic systems for renewable energy conversion reactions such as CO_2 reduction, water splitting and purification.*

Stephan N. Steinmann

Dr Stephan N. Steinmann is a CNRS researcher at the Ecole Normale Superieure de Lyon (France). After his PhD thesis on the development of dispersion corrections to standard density functional approximations in 2012 at the Ecole Polytechnique Federale de Lausanne (Switzerland), he went for a post-doctoral stay to Duke University (USA), developing electronic structure methods. Back in Europe since 2014, he has been developing advanced methods to treat heterogeneous electrocatalysis and the metal/liquid interface in general. Concomitantly, his current research is devoted to strong collaborations with experimental groups from academia and industry.

renewable source of energy, and its depletion within the next century could pose grave consequences if suitable alternatives are not found on time.[2] In addition, fossil fuel combustion is also a major source of CO_2, along with other noxious pollutants like soot, SO_x, and NO_x that further exacerbate environmental issues.

Electro- and photocatalytic energy conversion presents an attractive pathway to convert earth abundant molecules (*e.g.* H_2O, CO_2, or N_2) into high-value products and fuels (*e.g.* H_2, hydrocarbons, oxygenates, or NH_3). While sustainable conversion can be achieved by tapping into renewable energy sources, the viability of this process is contingent on the development of selective, robust and affordable catalysts that allow faster reaction rates to occur at lower overpotentials. The search for high performance catalysts, especially those without precious metal content, has attracted intensive research interest.[3] MXenes, a contemporary family of 2D materials based on transition metal carbides or nitrides, have shown interesting properties and promise in catalytic energy conversion.[4] So far, of the 54 MXenes proposed to exist *in silico*, only 22 of them have been experimentally realised (Fig. 1). One of the challenges in MXene synthesis is the instability of some of its constituents in strong HF etchants, particularly nitrogen and transition metals reactive to fluorine.[5] More recently, milder synthesis routes using *in situ* HF generated from fluoride salts in acids have been demonstrated.[6,7]

In this review, we will discuss the latest promising research on MXenes in the field of electro- and photocatalytic energy conversion, based on the strategy of theory-guided materials design. First, the fundamentals of catalytic energy conversion will be elaborated, including the H_2 evolution reaction (HER), O_2 evolution reaction (OER), O_2 reduction reaction (ORR), CO_2 reduction reaction (CO_2RR) and N_2 reduction reaction (N_2RR). The key properties of MXenes relevant to electro- and photocatalysis will also be discussed. A critical appraisal of the state-of-the-art research using MXenes as catalysts in the above reactions will follow, including both theoretical and experimental aspects. Using computational chemistry to guide materials design has the potential to accelerate catalyst development by uncovering broader governing principles and providing rational design guidelines. In the process, we will also be pointing out current limitations in theoretical models, existing scientific gaps and future research directions for this field.

Zhi Wei Seh

*Zhi Wei Seh is a scientist and NRF fellow at the Institute of Materials Research and Engineering, A*STAR. He received his BS and PhD degrees in Materials Science and Engineering from Cornell University and Stanford University, respectively. His research interests lie in the design of new materials for energy storage and conversion, including advanced battery and electrocatalyst systems. He has published in top journals such as Science, Nature Communications, Nature Energy and Nature Catalysis, and has also received numerous awards including the Highly Cited Researchers (Clarivate Analytics), Emerging Investigators (Journal of Materials Chemistry A), and Innovators under 35 Asia (MIT Technology Review) awards.*

2. Fundamentals

2.1 Basic concepts

Electrocatalysis exploits the thermodynamic and kinetic tuning of electrochemical reactions occurring on electrode surfaces as a function of the applied external voltage. An electrocatalyst modifies the catalytic reaction rate compared to solution electrochemistry or an inert electrode, by providing favourable reaction sites, altering adsorption energies and/or introducing alternative reaction pathways. Therefore, faster product formation can be achieved at lower overpotentials. Modifications in exposed facets,[9] surface functionalisation,[10] size[11–13] and doping/co-catalyst addition[14,15] are common strategies to enhance electrochemical activity and selectivity. Depending on the target reaction, MXenes can be suitable electrocatalysts due to their high electronic conductivity and optimal adsorption strength for key reaction intermediates.

In photocatalysis, the driving force arises from electron/hole pairs generated in semiconducting materials upon light irradiation. The additional step of photocarrier generation makes photocatalysis generally less efficient than electrocatalysis due to the associated energy losses. Important strategies to improve photocatalyst performance usually involve bandgap alteration,[16] addition of co-catalysts,[17–19] or the formation of a cascading junction (*Z*-scheme) structure[20–22] aimed at enhancing light absorption and promoting photogenerated carrier separation.[23] MXenes can be a prime choice for co-catalysts as their Fermi level is compatible with the Fermi levels of popular wide-bandgap photocatalysts like TiO_2 and ZnO, thus encouraging electron migration to MXene surfaces and simultaneous formation of a Schottky barrier at the interface to prevent back-flow.[18]

Before going into the details of electro- and photocatalytic processes, there are several fundamental terms that need to be defined.

Overpotential describes how much additional voltage above the thermodynamic requirement is needed to drive an electrochemical reaction. Expressed as a potential difference, overpotential is considered as one of the primary metrics in evaluating the catalytic activity as it is strongly related to the redox reaction kinetics and the overall energy efficiency of the process. Experimentally, it is determined by the onset potential at which a redox event is observed, usually marked by a significant rise of the current density compared to the baseline (non-redox) level. Electro- and photocatalytic reactions such as CO_2RR can be complicated, with multiple electron transfer steps involving different intermediates and overpotentials.[24] It is common to take the largest overpotential (*i.e.* the most difficult) of those

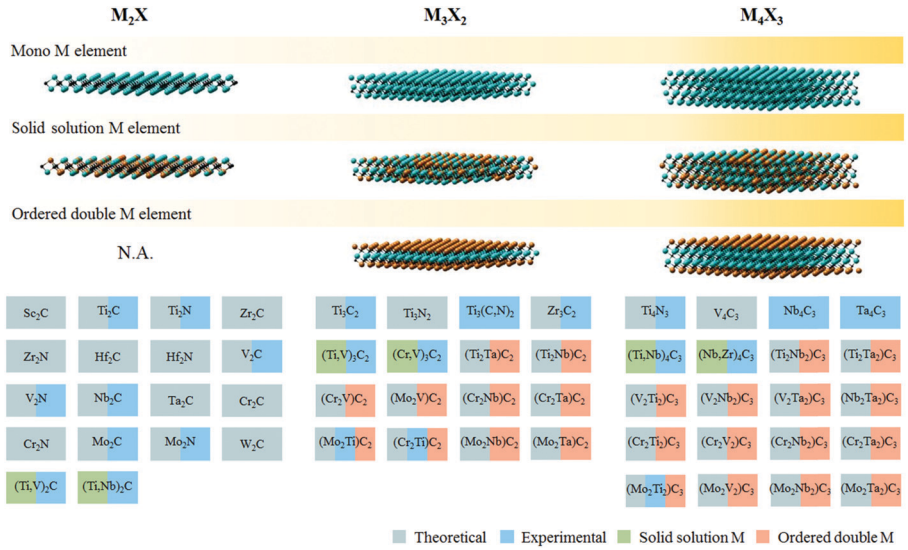

Fig. 1 Different types of MXene discovered so far, both theoretically and experimentally. Adapted with permission from ref. 4 Springer-Nature, Copyright 2017. Updated with newly synthesised MXenes from ref. 7 and 8.

individual steps to be the overall redox overpotential. An excellent catalyst should display an overall overpotential value close to zero.

Faradaic efficiency (FE) describes how efficient a catalytic system is in using electron input to facilitate a particular chemical reaction. In catalysis, FE is usually calculated by comparing the e_{output}, estimated based on the amount of product generated (or reactant consumed), with the actual e_{input} as measured by a coulombmeter or a potentiostat. A real catalytic reaction usually shows FE less than unity, as Faradaic losses can be incurred when electrons or ions participate in unmonitored side reactions. Comparison of FE among different products can serve as an insightful indicator for both energy efficiency and product selectivity, especially important for CO_2RR where product selectivity is a critical challenge.

Turnover number (TON) describes the intrinsic activity of a catalyst. It is usually defined as the total number of reactant molecules converted (or the total number of product molecules generated) per active site. TON is also often used to describe the "recyclability" of a catalyst, which is calculated by the number of molecules of the reagent that a molecule of catalyst can convert before it becomes inactive. In both cases, an ideal catalyst should have a very large TON, approaching infinity. Sometimes, the term turnover frequency (TOF) is used, which is simply TON per unit time. TOF describes the number of catalytic conversions that occur at the active centre per unit time, which also gives information on the overall kinetics. Thus, the higher the intrinsic reaction rate, the higher the TOF value.

Tafel plot/equation relates the rate of electrochemical reaction on a particular catalyst to the applied overpotential:

$$\eta = b \times \log\frac{i}{i_0} \quad (1)$$

$$b = \frac{2.303RT}{\alpha F} \quad (2)$$

where η is the overpotential, b is the Tafel slope, i is the current density, and i_0 is the exchange current density. The constants and coefficients used in the equation are R, T, F and α, representing the gas constant, temperature, Faraday's constant and reaction transfer coefficient, respectively. Two of the most important measures in the Tafel equation are b and i_0, as they can provide insights regarding the interaction between the reactant/electrolyte and the catalyst surface, as well as the rate-determining reaction step. Experimentally, the values of b and i_0 can be obtained by plotting the applied overpotential against the logarithm of observed current density. The Tafel slope b is the overpotential difference required to increase the observed current density by a decade (thus the unit V dec^{-1}), and i_0 is obtained by extrapolating the Tafel plot to intersect the "log i" axis at zero η. Smaller b and larger i_0 values are indicators of a good catalyst, implying a larger reaction transfer coefficient and better binding between the reactants/electrolyte and catalyst. Tafel slope values, subject to limitations, can also be used as indicators of reaction pathways and rate determining steps in electrochemical reactions. For example, a multi-step reaction with the rate determining chemical step preceded by two 1-electron electrochemical steps should display a Tafel slope of around 30 mV dec^{-1}.[25]

The Sabatier principle states that the adsorption between the catalysts and reactants should be neither too weak nor too strong.[26] When the adsorption is too weak, it becomes difficult to bind the reactants onto the catalyst surface, and no reaction would take place. On the other hand, very strong adsorption causes the reactant to be too strongly bound, slowing down the product desorption step, and sometimes leading to rapid catalyst deactivation.[27] Hence, an optimal catalyst should bind the reactants just strong enough to allow surface adsorption of the reactant, while still allowing facile desorption of the intended products. Taking a relatively simple HER as an example, the catalytic activity (expressed as i_0) of the elementary steps (Volmer, Tafel or Heyrovský) is exponentially proportional to the partial

pressure of hydrogen (p_{H_2}) and the standard Gibbs free energy of adsorption of atomic hydrogen (ΔG_H) by:[28]

$$i_0 \propto \left(p_{H_2}{}^{1/2} \exp\frac{-\Delta G_H}{2kT}\right)\left(1 + p_{H_2}{}^{1/2} \exp\frac{-\Delta G_H}{2kT}\right)^{-1} \quad (3)$$

where k is the Boltzmann constant and T is the temperature in Kelvin.

Plotting $\log i_0$ against ΔG_H results in a triangle that yields a maximum value of i_0 when ΔG_H is close to 0, and rising and falling $\log i_0$ when $\frac{\Delta G_H}{2kT} \ll 1$ (very strong *H adsorption, * denotes an adsorption site on the electrode) and $\frac{\Delta G_H}{2kT} \gg 1$ (*i.e.* very weak *H adsorption), respectively, giving rise to a 'volcano plot'.

2.2 Computational methods

Density functional theory (DFT) is frequently exploited to calculate the adsorption energy based on the differences between the energy of a ''clean'' atomic surface model plus half the energy of a H_2 molecule, representing a proton/electron pair. This model is known as the computational hydrogen electrode (CHE).[29] In combination with DFT computations for the intermediates (*e.g.* the energy of hydrogen bound onto the same surface model), thermodynamic overpotentials can be estimated at low computational cost. The thermodynamic overpotential is defined as the potential at which each electrochemical step (coupled proton/electron transfer) is thermo-neutral. These overpotentials can then be plotted as a function of a descriptor (*e.g.*, the d-band centre or the adsorption energy of a particular intermediate) to obtain a volcano plot. Though simple, volcano plots have proven to be a powerful tool that can predict the activity of different materials in catalysing various reactions.[3,30,31]

In its most commonly used CHE formulation, neither electrolyte presence nor electrode polarization due to the applied electrochemical potential is taken into account. It also assumes that no additional kinetic barriers exist, *i.e.* if a reaction is thermodynamically favourable at a given potential, it will also occur at a high rate. These assumptions, which simplify the computational work significantly, often provide correct trends,[32–34] although they cannot capture the details of the electrochemical processes.[35–37] Furthermore, for complex reactions, where chemical and electrochemical steps have to be considered, microkinetic simulations are necessary to estimate the rate of the electrochemical reactions, rather than taking the thermodynamic overpotential as provided by CHE as a proxy for the activity of a given catalyst.[38,39]

In order to lift the approximations of CHE, transition states for all processes need to be determined, which is particularly challenging for electrochemical reactions.[40,41] Second, the electrochemical potential needs to be included explicitly, which is equivalent to simulating electrode surfaces in the presence of a surface charge. Third, the solvent needs to be modelled as well. The computationally most efficient approach is to rely on an implicit solvent/electrolyte,[42–44] which comes at the cost of neglecting ''direct'' (*i.e.* chemical) effects of the solvent, such as the competition of the adsorption between reactants and the solvent or the assistance of solvent molecules in breaking bonds.[45] Alternatively, aqueous electrolytes are often approximated as ice-like layers,[46,47] which is very cumbersome for studying various reaction intermediates, as the (arbitrary) placement of adsorbates into or under these ice-like layers is associated with uncontrolled effects on their properties. Furthermore, for non-aqueous solvents, no obvious organization for placing explicit solvent molecules is currently available. All these challenges explain why the simplistic CHE model, with its success in predicting activity trends, continues to be highly popular.

3. Properties of MXenes

In order to elaborate about MXenes, one has to understand a special family of the layered MAX phases. The acronym MAX comes from the materials' composition, $M_{n+1}AX_n$ (n = 1, 2 and 3), where 'M' stands for early transition metals such as Sc, Ti, Cr, Nb, V, Mo and so on, 'A' is a group IIIA or IVA element, and 'X' represents C and/or N. MAX is composed of $M_{n+1}X_n$ face-sharing octahedral layers and interlayer cation A, resulting in a hexagonal $P6_3/mmc$ structure, the same symmetry as graphite (Fig. 2A). By etching out the interlayer cations A, a graphene-like 2D transition metal carbide/nitride $M_{n+1}X_nT_x$ (here T represents the surface termination groups such as fluorine, oxygen or hydroxyl) is obtained, and the name MXene was given due to their remarkable similarity to graphene and the relation to the MAX phase.[5]

The relatively strong metallic M–A bonds in MAX phases suggest that the mechanical method is not suitable to exfoliate the $M_{n+1}X_n$ layers. However, the distinct chemical reactivity between M–A and M–X bonds make selective etching plausible. Thus the first reported carbide MXene, $Ti_3C_2T_x$, was obtained *via* aqueous hydrofluoric acid (HF) etching of Ti_3AlC_2 at room temperature (Fig. 2B).[5] The majority of other MXene phases were synthesized with a similar recipe, using either direct addition of HF or *via in situ* formation of HF (*e.g.* by adding LiF to HCl), sometimes at elevated temperature and/or prolonged heating.[4,6]

Most pristine (bare) MXenes show metallic characteristics.[48] The high conductivity can be linked to the redistribution of the outer M(1) atoms' 3d states from the broken M(1)–A bonds into delocalized M(1)–M(1) metallic-like bonding states placed in the window around the Fermi level (Fig. 2C).[49] The M(1) atoms are distinct from the inner M(2) atoms that interact more closely with the X atoms.

Further delamination of the MXene layers can be achieved by intercalation strategies, using sonication in moieties such as dimethyl sulfoxide, tetrabutylammonium hydroxide or amines.[4,6,50,51] Other synthetic methods, such as etching MAX powders in molten fluoride salt at high temperature and in an inert environment, or chemical vapour deposition (CVD), have so far been demonstrated only on limited types of MXenes.[52–56] We note that, while requiring high vacuum and high temperature, the CVD growth method is particularly promising for extra-large grain growth of bare MXenes that may be of interest in energy storage application.[52,53] Nitride variant of MXenes is also obtainable *via* ammoniation of the carbide MXene.[8]

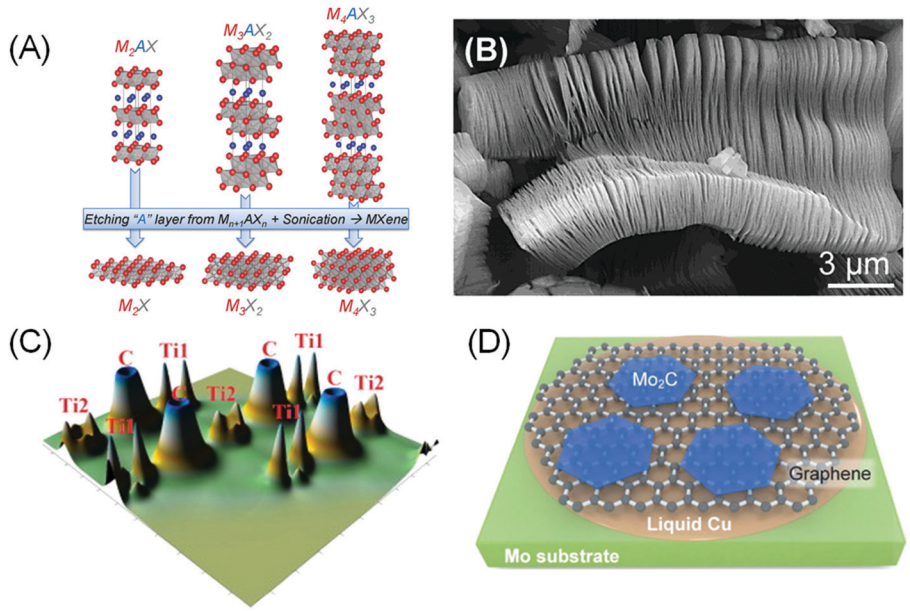

Fig. 2 (A) Structure of MAX and the corresponding MXenes after etching an "A" layer and sonication. Reprinted with permission from ref. 58 Copyright 2013 Wiley-VCH Verlag GmbH & Co. KGaA. (B) Scanning electron micrograph of $Ti_3C_2T_x$ after HF etching of Ti_3AlC_2. Reprinted with permission from ref. 59 Copyright 2012 American Chemical Society. (C) Calculated valence electron density of bare Ti_2C. Ti1 refers to the outermost Ti atoms that have direct bonds with 'A' atoms, while Ti2 represents inner Ti atoms that interact only with X atoms. Reprinted from ref. 49 Copyright 2012, with permission from Elsevier. (D) Schematic showing CVD growth of bare Mo_2C MXenes on a molten Cu on Mo substrate from a CH_4 precursor. A graphene underlayer was formed *in situ* at a high CH_4 flow rate. Reprinted with permission from ref. 52 Copyright 2013 Wiley-VCH Verlag GmbH & Co. KGaA.

So far, among the 70 odd MAX phases, only Al-containing ones have shown successful conversion to MXenes.[4] This led to the exploration of other, non-MAX layered materials, like $Zr_3Al_3C_5$ that have been shown to form $Zr_3C_2T_x$ after HF etching.[57] Unlike the case for the MAX precursor, where only a single layer of 'A' element is removed, multiple layers of atoms are removed for the non-MAX precursors (*e.g.* 3 Al–C layers for $Zr_3Al_3C_5$).

To date, 22 MXenes have been successfully synthesized and dozens more theoretically predicted.[4] However, producing single phase MXene monolayers remains highly challenging for many MXene compositions, and less hazardous synthesis procedures are still under investigation.

3.1 Surface terminations

To maintain charge balance, surface terminations quickly form on the "dangling" M(1) atoms during the etching of A atoms in aqueous HF solutions. –OH, –O, and –F are the most common species that can be observed filling the T_x surface termination sites in wet-etched MXenes. An exception is MXenes produced *via* the CVD method, of which bare Mo_2C has been grown on a molten Cu/Mo substrate from a CH_4 precursor.[52] Larger and thinner Mo_2C grains were achieved by increasing the CH_4 flow rate, which results in *in situ* formation of a graphene underlayer that improves the crystallinity of Mo_2C (Fig. 2D).

Precise characterization on the surface coverage and ratios of termination groups using X-ray techniques remains challenging due to the intrinsic low-scattering strength of the light elements. Solid state nuclear magnetic resonance (NMR) spectroscopy is one potential solution, as it has been successfully used to quantify the surface termination composition on $Ti_3C_2T_x$ MXene.[60] More importantly, the study indicates that the ratio of T_x surface termination species can be tuned by adjusting the synthesis method. DFT calculations also indicate that the tuneability of the T_x population is also related to the different metal species in MXenes, which governs the stability of the M–T_x interaction.[61,62]

Being the outer-most layer, the composition of T_x significantly influences MXene's physical and electronic properties. For example, –O terminated MXenes have been calculated to have smaller lattice parameters and thinner interlayer thickness than –F and –OH terminated variants, leading to higher mechanical strength.[63] The presence of T_x termination also makes MXenes more semiconducting. The source of this electronic property alteration is linked to the distinct electron orbital hybridization that yields bandgap variations. For example, the bandgap of Sc_2CT_x MXene was found to be dependent on the T_x species in the order of $Sc_2CO_2 > Sc_2CF_2 > Sc_2C(OH)_2$.[63] Generally –F and –OH have similar effects on the electronic structures because both can only receive one electron, but –O differs significantly because it readily demands two electrons.[63] It is also shown that –O functionalisation is most favourable for high Li-ion capacity, superior to those with –F and –OH terminations, as Li prefers to adsorb on O.[64,65] In some other application areas, such as heavy metal ion adsorption, –OH terminated MXenes are preferred.[66]

The T_x composition was also found to affect surface adsorption and magnetisation behaviour. For example, –O terminated $Ti_3C_2T_x$ exhibits a near zero G_H of 0.003 eV while bare and –F terminated $Ti_3C_2T_x$ give high values of −0.927 and 1.995 eV, respectively.[18] Moreover, –OH terminated $Ti_3C_2T_x$ is calculated to show stronger CO_2 adsorption than –F terminated ones.[19] In general, the experimentally hardly avoidable surface termination by T_x suppresses

the magnetism and electronic conductivity in MXenes. For example, the semi-metallic ferromagnetic behaviour of bare Cr_2C has been shown to become semiconducting antiferromagnetic upon –F, –OH and –H functionalization.[67] Similarly, other properties such as optical, thermal and charge transport are effectively modified by the presence of surface functionalizations.[68]

3.2 Carbide *vs.* nitride MXenes

The relatively more electronegative nitrogen compared to carbon at the MXene X sites gives stronger bonding to the electropositive M, thus variations in physical and electronic properties related to the shorter M–M and M–X interatomic distances are expected. For example, bare $Ti_{n+1}N_nT_x$ has been calculated to have smaller lattice constant and monolayer thickness compared to $Ti_{n+1}C_nT_x$, accompanied by larger in-plane Young's modulus.[69] It is interesting that $Ti_{n+1}N_nT_x$ MXenes, including –O terminated ones, have higher density of states (DOS) at the Fermi level, as opposed to carbide MXenes.[70] These findings lead to predictions of higher electronic conductivity and more catalytically active surface on nitride MXenes.

Despite their immense promise, nitride MXenes are generally more difficult to obtain due to less stable M–N layers in the etching solution and higher formation energy. Nevertheless, an etching strategy to produce Ti_2NT_x by exploiting the K^+ ions that can intercalate and weaken the M–X layers has recently been proposed.[7] An alternative strategy is to obtain nitride MXene *via* ammoniation of the carbide MXene, for example Mo_2NT_x synthesized from Mo_2CT_x is reported to exhibit 3 orders of magnitude higher electrical conductivity than the corresponding carbide.[8] Although limited by difficulties in synthesis, we expect that nitride MXenes will continue to be the subject of intense experimentation to exploit their superior electronic and physical properties.

3.3 Effect of metal species

Many interesting properties of MXenes arise from the open d orbitals in the M transition metal. Thus, modification of M with different metal species, either as solid solutions, ordered layers or ad-atoms, is expected to bring a dramatic change in their properties. The strong interaction between M and the adjacent T_x suggests that MXenes with different metals may energetically favour different functional groups. For example, –F and –O species are more commonly detected in $Ti_3C_2T_x$, whereas –F and –OH are more common for V_2CT_x.[61,62] Consequently, alteration of M species composition will bring about a significant change in the electronic properties of MXenes.[48] A more subtle change in the electronic structure has been predicted on MXenes with varying M but the same T_x preference, as seen in the increased bandgap in the order of $Ti_2CO_2 < Zr_2CO_2 < Hf_2CO_2$.[68] Addition of transition metal ad-atoms over the MXene layer has also been reported to yield interesting HER catalytic properties.[71]

The discovery of double-transition metal MXenes,[72] containing a sandwiched configuration of different M′ and M″ transition metal species, has enriched the family further. The metals can be either randomly distributed (*e.g.* $(Nb,Zr)_4C_3T_x$, solid solution[73]), or form ordered layers of M′–X–M″–X–M′ (*e.g.* $Mo_2TiC_2T_x$) or M′–X–M″–X–M″–X–M′ (*e.g.* $Mo_2Ti_2C_3T_x$[74]). The overall electronic properties will be highly dependent on the overall DOS near the Fermi level which contains both M′ and M″ partially filled d orbitals due to the degeneracy effect. This means double-transition metal MXene can be intrinsic semiconductors (like the ordered Mo_2TiC_2 and Cr_2TiC_2[74,75]) or a semi-metal (like $Ti_2MnC_2T_x$[76]). It is interesting that $Ti_2MnC_2T_x$ is still found to be ferromagnetic in the ground state regardless of its surface terminations,[76] while surface terminations have been shown to quench magnetism in single MXenes like Ti_2CT_x.

Understandably, the outer M′ atoms still play a more important role in MXene's surface behaviour compared to inner M″. For example, $Mo_2TiC_2T_x$ shows Li adsorption behaviour closer to $Mo_3C_2T_x$, rather than the isostructural $Ti_3C_2T_x$, thus the former shows larger capacity when applied as a Li-battery electrode.[74] The current investigation on double transition metal MXenes is very limited, but it is expected to expand rapidly. Khazaei *et al.* proposed that many compositions are topological insulators due to their large spin orbital coupling between metal elements that can be widely applied in many energy applications such as thermoelectrics.[77]

3.4 Effect of layer thickness

Due to the higher volume to surface ratio, the stability of MXenes generally increases with increasing layer thickness, such that $M_2XT_x < M_3X_2T_x < M_4X_3T_x$, in agreement with the experimental observation on the better stability of $Ti_3C_2T_x$ compared to Ti_2CT_x.[48] The effect of layer thickness on mechanical properties is investigated by first-principles calculations, and highest Young's moduli for the thinnest MXene are obtained from a comparison of Ti_2C, Ti_3C_2 and Ti_4C_3.[78] The equilibrium bond strength calculations indicate that Ti_2C has the shortest Ti–Ti distance but the longest Ti–C bond among the three.[49] As surface properties mainly depend on the outer layer atoms, different layer thicknesses do not induce a significant effect on their preferred surface functionalization, *e.g.* $Ti_{n+1}C_nT_x$ show similar T_x preference of –O > –F > –OH, regardless of the value of n.[78] However, distinct metal d band degeneracy was observed on MXenes with the same atomic constituent but different n, thus displaying significantly different electronic structures.[79] DFT calculations found that the DOS near the Fermi level generally reduces with increasing n for pristine $Ti_{n+1}X_n$.[49] Interestingly, bulk $Ti_3C_2T_x$ (n = 2) displays much smaller electrical resistivity than Ti_2CT_x (n = 1) possessing similar surface functionalization, probably due to the increasing difficulty for electron hopping in between the layers when n is smaller.[59] Due to the varying accessibility and tuneability of the active sites, different values of n have also been shown to cause variations in the HER activity.[11,80]

With appropriate delamination, MXenes can be obtained as a monolayer or multiple layers; the inter-layer spacing can be tuned by intercalation using multivalent cations, water or organic molecules. The transition metals with partially filled d-orbitals can have different oxidation and spin states, bringing up a vast range of interesting properties. The hydrophilic nature of T_x leads to stable water-based solutions or suspensions, which facilitates applications requiring coating or thin film fabrication.

While it has been established that most MXenes show metallic-like behaviours, the actual bulk conductivity depends greatly on the preparation method. Milder etching and delamination conditions generally result in higher bulk conductivity,[81] and so is more thorough removal of intercalated species.[82] In summary, the flexibility and tuneability of atomic composition and surface functionalization are key to the excellent electronic, physical and surface properties of MXenes, making them unique among the 2D materials reported so far.

In the next few sections, we will discuss how the excellent properties of MXenes can be exploited to enhance catalytic conversion to various value-added chemicals and fuels.

4. MXene catalysts for hydrogen evolution

4.1 Electrocatalytic hydrogen evolution reaction (HER)

As one of the two half-reactions of electrochemical water splitting, HER provides a cornerstone in the exploration of other, more complex electrocatalytic processes that involve multiple electron transfer. In brief, the mechanism for HER can be separated into three distinct elementary reactions under acidic conditions:

Volmer (adsorption/discharge reaction)

$$H^+ + e^- + * \rightarrow *H \quad (4)$$

Tafel (combination reaction)

$$2*H \rightarrow H_2 + 2* \quad (5)$$

Heyrovský (ion + adsorbed *H reaction)

$$H^+ + *H + e^- \rightarrow H_2 + * \quad (6)$$

Under alkaline conditions, a different Volmer and Heyrovský mechanism is proposed due to low H^+ ion concentration in the electrolyte:Volmer (alkaline)

$$H_2O + e^- + * \rightarrow *H + OH^- \quad (7)$$

Heyrovský (alkaline)

$$H_2O + *H + e^- \rightarrow H_2 + * + OH^- \quad (8)$$

Regardless of the steps taken, the overall rate of reaction is highly dependent on the hydrogen adsorption free energy G_H. Recalling the Sabatier principle, if the hydrogen binds to the surface too weakly, the adsorption (Volmer) step will be difficult. On the other hand, the desorption step (Tafel or Heyrovský) becomes rate-limiting with overly strong hydrogen bonding. Beyond this qualitative assessment, Nørskov *et al.* found that the activation energies (E_a) of various bond-dissociations are linearly correlated with the respective adsorption strengths (ΔE) on a number of different metals of similar surface geometry according to the Brønsted–Evans–Polanyi relationship.[83,84] The fact that the relationship between E_a and ΔE is more dependent on the surface structure of the reaction site rather than the type of molecules means that there exists a universal relation for various activities observed on different catalysts.[85]

Nørskov's finding opened a new dimension in catalytic research and now DFT is routinely employed to predict the reactivity of catalysts, based on the calculated binding strength to a particular surface structure. In the quest to search for a prominent HER electrocatalyst amongst MXenes, a holistic consideration of intrinsic metal orbital hybridization, surface terminations as well as layer thickness is required. MXene's high DOS near the Fermi level, constructed from the partially filled d orbitals of M(1) and M(2), is expected to favourably interact with the hydrogen 1s orbital. This is advantageous compared to other, rather inert, 2D materials such as MoS_2,[86] as the entire basal plane of MXene's highly anisotropic monolayered structure has the potential to act as active sites for hydrogen adsorption.[10,87]

DFT is an ideal tool to assess MXene's potential for HER electrocatalysis, as it provides a framework for rapid, precise, systematic and yet qualitatively correct predictions of the catalytic performance. The primary metric is G_H, and volcano plots based on calculated G_H values are then constructed to aid in material screening (Fig. 3A).[80,87] In the case of MXenes, the composition and role of T_x surface functional groups for *H adsorption sites need to be clarified and taken into account for a more realistic approximation. In M_2XT_x type MXenes, –O or –OH was found to be the preferred T_x species, with five MXenes with theoretical HER overpotential under 100 mV identified: $Sc_2C(OH)_2$, $Mo_2CO_{1.75}(OH)_{0.25}$, Hf_2NO_2, Nb_2NO_2 and V_2NO_2 (Fig. 3B).[87] Ling *et al.* further observed that the HER overpotential calculation may be simplified as it is directly related to the electron gain of the –O T_x group from various transition metals in M_2CO_2 systems.[88] These theoretical works enable the rational selection of promising MXene catalysts for further experimental testing.

Using theory-guided materials design, Handoko *et al.* demonstrated Mo_2CT_x MXenes that can achieve a HER current density of 10 mA cm^{-2} at 190 mV overpotential (Fig. 3C). It was found that the HER overpotential and activity of MXenes vary significantly with changing T_x species composition.[10] In particular, –F species was found to be particularly detrimental to MXene's HER activity: $Ti_3C_2T_x$ obtained from etching in 50% HF (with 70% –F coverage on the basal plane) exhibited >350 mV worse HER overpotential compared to the mild LiF–HCl etched ones (with 18% –F coverage). This observation is consistent with separate DFT investigations of Ti, V and Nb-based MXenes that suggest that –O functionalization weakens *H adsorption of bare MXenes towards an ideal G_H value.[79] This is a strong indicator that the T_x species plays a dominant role in the catalytic activity of MXenes. For example, the HER activity variation of $Mo_2CT_x > Mo_2TiC_2T_x > Mo_2Ti_2C_3T_x$ is more closely correlated with the extent of –F coverage on their surfaces than the outer metallic species (Fig. 3C), as Mo is the outer M′ species in all three cases above.[10]

Several other promising theoretical and experimental approaches have been explored to enhance the HER activity of MXenes, such as:

(1) Controlling the surface functionalization. In particular, replacing –F termination with other moieties such as –O or –OH with suitable *H adsorption strength as described in the case of $Ti_3C_2T_x$.[10]

(2) Interlayer delamination. Delamination of MXene interlayers increases the basal plane accessible for HER. This effect

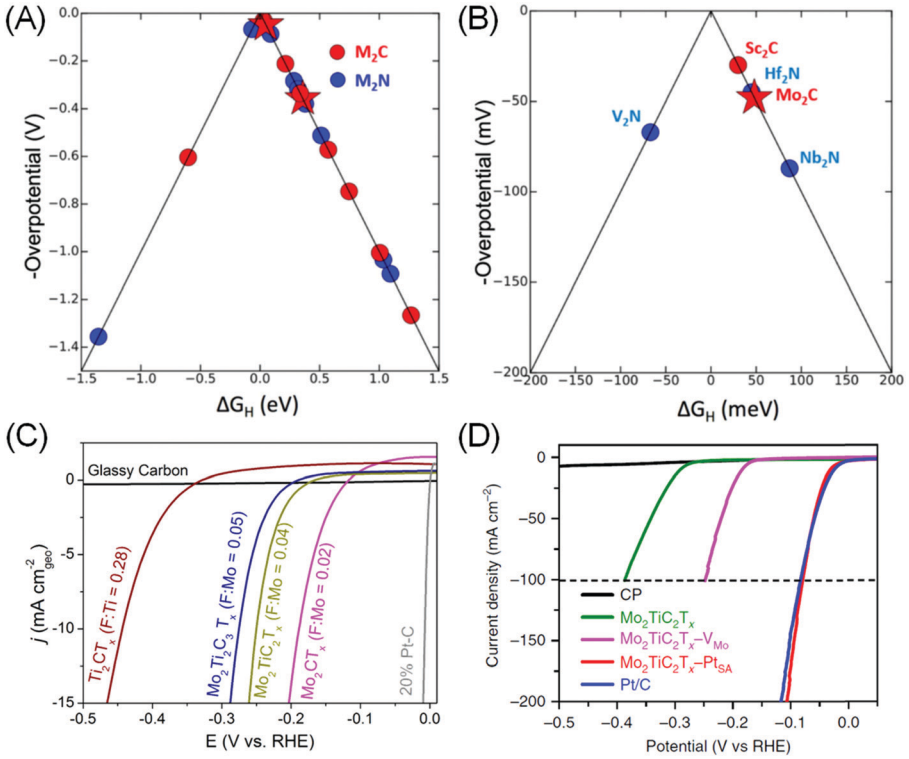

Fig. 3 (A) Volcano plot showing calculated ΔG_H and theoretical overpotentials for different M_2XT_x MXenes and (B) zoom-in to the top of the volcano plot. (a and b) Reprinted with permission from ref. 87 Copyright 2012 American Chemical Society. (C) Linear scanning voltammetry (LSV) of various MXenes containing different –F termination contents in 0.5 M H_2SO_4 electrolyte. From ref. 10. (D) HER polarization curves of carbon paper (CP), $Mo_2TiC_2T_x$ MXene, $Mo_2TiC_2T_x$ with Mo vacancy ($-V_{Mo}$), $Mo_2TiC_2T_x$ with embedded Pt single atom ($-Pt_{SA}$) and Pt/C (40%) in 0.5 M H_2SO_4 solution. Reprinted by permission from ref. 15 Springer-Nature, Copyright 2018.

has been demonstrated on Mo_2CT_x, where the overpotential to achieve 10 mA cm^{-2} current density can be reduced by 30 mV after delamination.[10] The improved overpotential indicates that the basal planes of Mo_2CT_x are catalytically active towards HER, unlike in the case of 2H-phase MoS_2, where the edge sites have been shown to be more active.[86] Alternatively, the interlayer delamination may have also improved the electron hopping to the basal plane.[89] A similar improvement in HER overpotential has also been demonstrated on Ti_2CT_x after delamination treatment in *N*-methyl-2-pyrrolidone.[87,90]

(3) Morphology modification and interfacial coupling. For example, specially shaped $Ti_3C_2T_x$ nanofibres etched from Ti_3AlC_2 fibres show a much lower HER overpotential of 169 mV and a smaller Tafel slope of 97 mV dec^{-1} compared to $Ti_3C_2T_x$ sheets.[91] Interfacial coupling between MXene and carbon or other 2D materials, like reduced graphene (rGO) or MoS_2, has also shown enhanced HER activity. A lower HER overpotential of 236 mV was observed on Mo_2C/graphene compared to 320 mV for bulk Mo_2C.[52] Separately, nanohybrids of MoS_2/Ti_3C_2/C composites show a lower HER overpotential of 135 mV compared to 352 mV for MoS_2/rGO without MXene.[92] The reasoning for the improved HER activity has been linked to the lowered Schottky barrier contact.[93,94]

(4) Chemical modification such as addition of ad-atoms or vacancies. Ling *et al.* proposed to introduce an electron donor onto the surface of V_2CO_2, to weaken its high hydrogen bonding strength to the surface O, so as to enhance the HER activity.[95] Addition of Fe, Co and Ni transition metal promoters was found to induce significant charge transfer between the promoters to the surface O, leading to less charge transfer between O and H and increased G_H closer to 0 eV. The most electropositive Fe was found to induce the strongest charge transfer to O, thus increase the G_H with the largest magnitude, followed by Co and then Ni.[95] In this way, it is possible to optimise the hydrogen adsorption strength by adding different metal ad-atoms. DFT is also an ideal tool in this case, as high-throughput screening combination of various MXenes and ad-atoms can be performed. Several combinations with G_H close to ideal were identified using this approach: Os–Ta_2CO_2, Ir–Sc_2CO_2, Ag–Nb_2NO_2, Re–Nb_2NO_2, and W–Nb_2NO_2.[71] Investigations into MXenes with metallic vacancies such as $Mo_{1.33}CT_x$ and $W_{1.33}CT_x$ were also reported to show promising HER activity.[96] Very recently, electrochemical treatment of $Mo_2TiC_2T_x$ MXene has resulted in Mo vacancy creation that increases its HER activity.[15] A similar treatment in the presence of Pt resulted in atomic Pt embedment in the $Mo_2TiC_2T_x$ lattice, achieving similar HER performance to the Pt/C catalyst, but with 40 times the mass activity (Fig. 3D).

Other approaches such as introducing structural strain on monolayer MXenes can also be promising. A strained surface has been shown to increase the energy of metal d-states and increase surface reactivity.[97] Strasser *et al.* demonstrated that

the catalytic activity of Pt–Cu alloys can be tuned by introducing surface strain through de-alloying.[98] Similar concepts may be applicable to MXenes, as strain has also been predicted to change the covalent character of the M–X bond and release d-electrons.[99] These newly formed states may also show favourable interactions with adsorbed *H and increase HER activity.

4.2 MXenes in photocatalytic HER

Although most bare and terminated MXenes have no or very small bandgaps, they have found their way as co-catalysts for photocatalytic HER due to their electrocatalytic HER performance. Additionally, MXenes are relatively water stable with a hydrophilic surface and metallic conductivity, making them a good substitute to noble metal co-catalysts. For example, a composite of 5 wt% MXene and a classic photocatalyst, TiO_2 (Fig. 4A), was reported to exhibit up to 940% higher H_2 production rate under visible light compared to bare TiO_2.[17]

Similarly, 2.5 wt% loading of –O/–OH terminated $Ti_3C_2T_x$ on CdS nanoparticles yields a 136.6 times higher H_2 production rate, superior to Pt/CdS under the same condition (Fig. 4B), presumably due to the better interfacial contact between MXenes and CdS.[18] Understandably, higher MXene loading does not necessarily result in better HER, as too much MXenes will block the light from the CdS semiconductor (Fig. 4C). In another example, $Ti_3C_2T_x$ and Ti_2CT_x were also shown to exhibit activity enhancement on g-C_3N_4.[100,101]

As metallic-like MXene could not have generated photo-carriers, the enhanced photocatalytic HER was attributed to the inherent catalytic activity of MXene in facilitating HER. Additionally, the formation of a Schottky barrier between MXene and the semiconductor encourages electron pooling and ameliorates charge recombination within the semiconductor band structure (Fig. 4D). The height of the Schottky barrier is proportional to the work function of the outer M′ transition metals, therefore higher photocatalytic activity can be further optimised by selecting a MXene–semiconductor composite pair with a suitable Fermi level.

We note that some MXenes, especially Sc and Y based ones like $Sc_2C(OH)_2$, are predicted to be good HER photocatalysts, as they have an indirect bandgap of around 2 eV and a conduction band minimum above the HER theoretical potential, thus opening up further opportunities.[102,103]

5. MXene catalysts for oxygen evolution and reduction

5.1 Oxygen evolution reaction (OER)

OER is the anodic half-reaction for overall water splitting. However, the substantial overpotentials required to overcome the kinetic barrier, even with the most efficient precious metal catalyst, make this process particularly challenging.[3] Additionally, OER (along with ORR) is also the major bottleneck step for rechargeable metal–air batteries.[104] Electrochemical OER is proposed to be a four-electron transfer process with the overall reaction as follows:

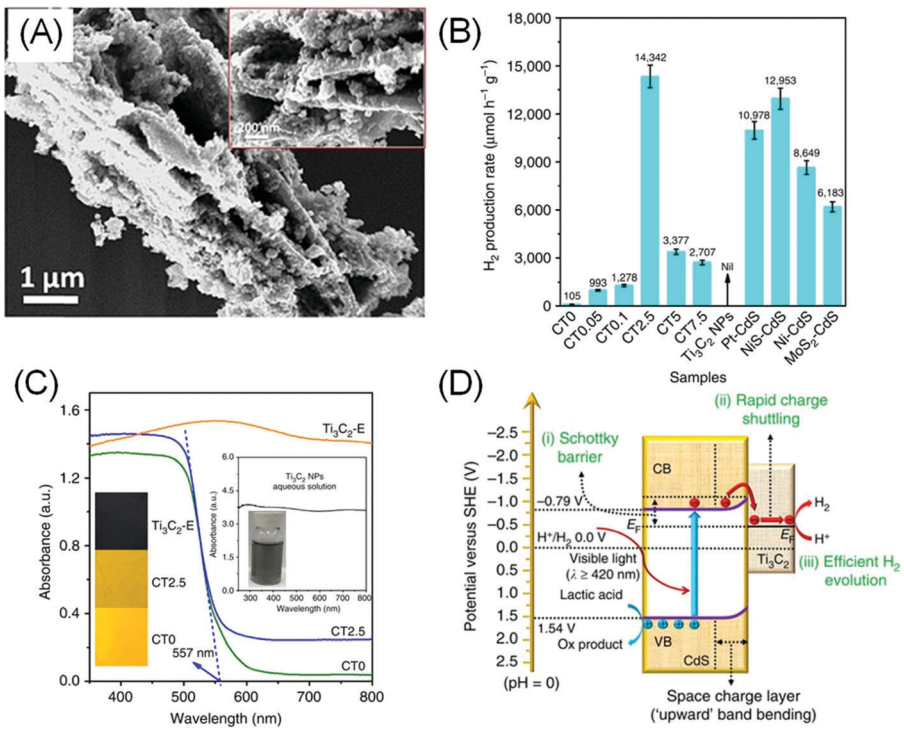

Fig. 4 (A) Electron micrographs of the $TiO_2/Ti_3C_2T_x$ (50 wt%) composite. Reprinted with permission from ref. 17 Copyright 2016 Wiley-VCH Verlag GmbH & Co. KGaA (B) photocatalytic H_2 evolution performance of the CdS/Ti_3C_2 composite (CT) with varying $Ti_3C_2T_x$/CdS mass loading ratio (0 to 7.5%) compared to bare $Ti_3C_2T_x$ and other composites of CdS with different catalysts. (C) UV-Vis diffuse reflectance spectra of the composite. (D) Proposed charge separation and transfer mechanism in the CdS/Ti_3C_2 system under visible light irradiation. (B and C) Reprinted from ref. 18 (CC BY 4.0).

In acidic electrolyte:

$$2H_2O \rightarrow O_2 + 4H^+ + 4e^- \quad (9)$$

In alkaline electrolyte:

$$4OH^- \rightarrow O_2 + 2H_2O + 4e^- \quad (10)$$

Due to its relatively positive potential (with respect to most metal oxidation potentials), it is proposed that an oxide layer always forms at the catalyst surface during OER,[105] sometimes even involving an increase in the formal oxidation state of the catalyst.[106–108] One of the more likely mechanisms is therefore the electrochemical oxide path (assuming acidic electrolyte):[109]

$$H_2O + * \rightarrow *OH + H^+ + e^- \quad (11)$$

$$*OH \rightarrow *O + H^+ + e^- \quad (12)$$

$$2*O \rightarrow O_2 + 2* \quad (13)$$

As can be seen, the mechanism of OER is more complicated than that of HER as it involves multiple steps and intermediates. Furthermore, the formation of oxide on a non-oxide catalyst surface needs to be taken into account as it affects the intermediate stability and OER reaction mechanism significantly. Various other reaction mechanisms based on catalyst behaviour in electrolytes have thus been proposed.[105,110] For example, an 'associative' mechanism (or metal peroxide route[109]) on intermediate *O binding energy surfaces like β-MnO_2 is proposed:

$$H_2O + * \rightarrow *OH + H^+ + e^- \quad (14)$$

$$*OH \rightarrow *O + H^+ + e^- \quad (15)$$

$$*O + H_2O \rightarrow *OOH + H^+ + e^- \quad (16)$$

$$*OOH \rightarrow O_2 + * + H^+ + e^- \quad (17)$$

Regardless of the route taken, a common feature is that the initial catalytic step involves the discharge of a hydroxide ion at a catalytically active surface site (*) to form a surface adsorbed hydroxide (*OH).[111] Subsequent steps in the reaction reflect the formation of surface intermediates that depends on the reaction conditions and catalyst surface. This is further complicated by the possibility of involvement from lattice oxygen atoms, as demonstrated by ^{18}O labelling experiment on ''nickelate'' ($MNiO_3$) and cobalt phosphate (CoPi) catalysts.[112,113]

Admittedly, OER is a more complex process than HER, and a universal ''activity descriptor'' for its activity is elusive, as different rate determining steps exist for different catalysts and reaction conditions. Seminal works by Trasatti suggested that the OER reactivity of simple oxides can be correlated with the standard enthalpy of transition from lower to higher oxides,[114] while Bockris and Ottagawa suggested that the catalytic OER activity on perovskites is inversely correlated with *OH binding energy.[110] Using DFT calculation, Rossmeisl *et al.* suggest that *O binding energy is a more suitable descriptor, putting RuO_2 at the apex of the volcano plot.[115] More recently Suntivich *et al.* proposed, through molecular orbital theory (MOT) calculation, that the level of surface cation (e_g) occupancy in perovskite type AMO_3 is a suitable descriptor, as it determines the binding of intermediates to the transition metal M (Fig. 5A).[31,116]

By themselves MXenes have not shown efficient OER electrocatalytic activity to date. However, when coupled with other catalysts, a synergistic effect has been shown to significantly accelerate the oxygen evolution process.[117–119] As most OER catalysts are based on metal oxides, the associated low electrical conductivity of oxides (except for ruthenates) is a major bottleneck. The hybrid systems assembled with MXenes would result in unique nanostructures, as the metallic conductivity and hydrophilic surfaces of MXenes, as well as enhanced surface area of the hybrids, can effectively promote the charge transfer. Yu *et al.* created a 2D hierarchy of 80 wt% FeNi–LDH (*i.e.* layered double hydroxide)–$Ti_3C_2T_x$ achieving an onset overpotential of 240 mV and a low overpotential of 298 mV at 10 mA cm^{-2}.[118] This is superior to the 372 and 407 mV displayed by bare FeNi–LDH and $Ni(OH)_2$ respectively, and also to that of the benchmark RuO_2 (397 mV). Similarly, Ni–Co mixed metal sulphide (NiCoS) incorporated with $Ti_3C_2T_x$ also yields a more competitive OER rate than RuO_2 in terms of smaller overpotential and Tafel slope, and larger TOF (Fig. 5B–D). XPS measurement suggested that the NiCoOOH originated from NiCoS during OER acted as the active sites.[117]

5.2 Oxygen reduction reaction (ORR)

ORR is a fundamental reaction for many processes in biology, energy conversion or materials dissolution, including fuel cells and metal–air batteries.[104] Under acidic conditions, ORR can be described as a simple dissociation of adsorbed oxygen on the catalyst surface, followed by the formation of hydroxyl species *via* electron transfer and hydrogenation:[29]

$$O_2 + 2* \rightarrow 2*O \quad (18)$$

$$*O + H^+ + e^- \rightarrow *OH \quad (19)$$

$$*OH + H^+ + e^- \rightarrow H_2O + * \quad (20)$$

Alternatively, it is also possible for the protonation of the oxygen to occur first before the di-oxygen is being dissociated. This mechanism is termed the ''associative'' mechanism:

$$O_2 + * \rightarrow *O_2 \quad (21)$$

$$*O_2 + H^+ + e^- \rightarrow *OOH \quad (22)$$

$$*OOH + H^+ + e^- \rightarrow *O + H_2O \quad (23)$$

$$*O + H^+ + e^- \rightarrow *OH \quad (24)$$

$$*OH + H^+ + e^- \rightarrow H_2O + * \quad (25)$$

Nørskov *et al.* proposed that the ORR activity can be closely correlated with the binding strength of the two reaction intermediates, *i.e.* *O and *OH (Fig. 5E),[29,121] which remains valid even when the associative mechanism involving *OOH is included. This observation is rationalised later on by the discovery of the scaling relations of adsorption energies of similarly adsorbed intermediates.[122]

In alkaline electrolytes, another indirect mechanism involves electron transfer (tunnelling) to the solvated molecular oxygen cluster in the outer Helmholtz plane.[123] This mechanism explains

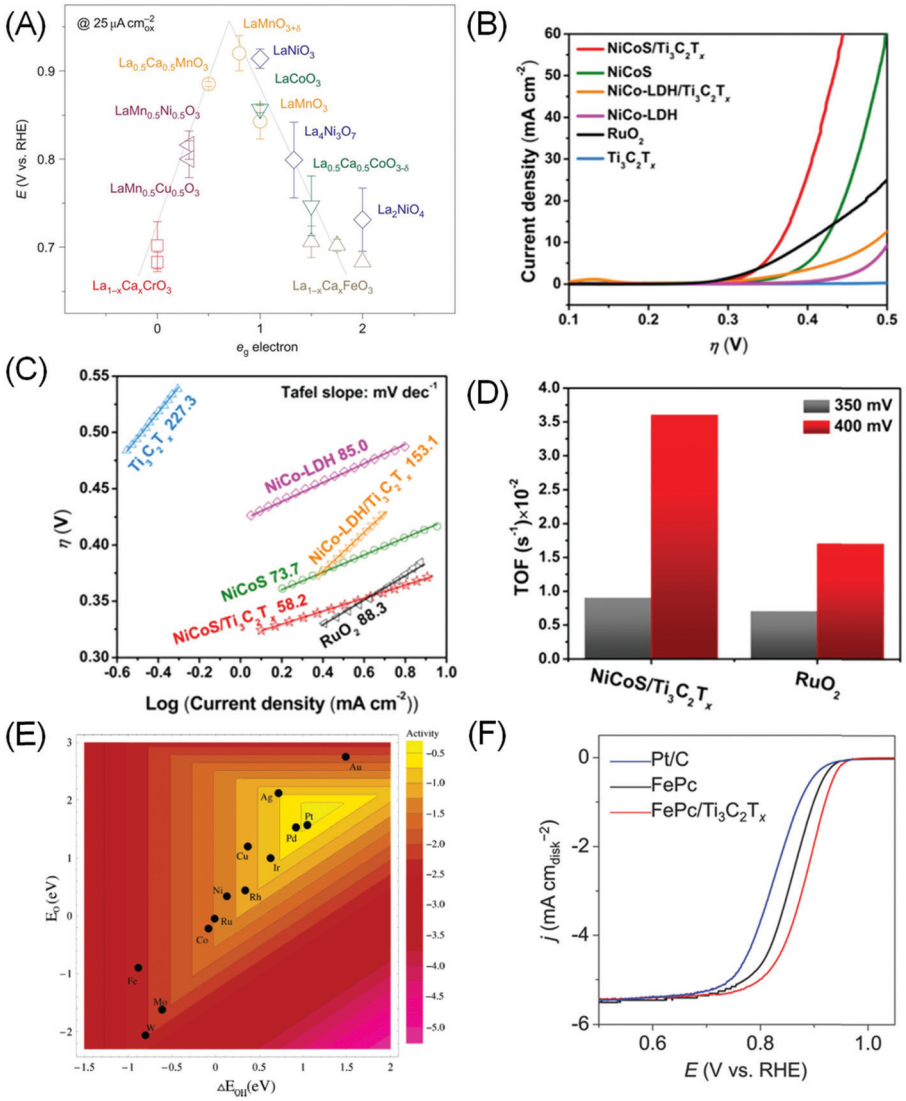

Fig. 5 (A) The relation between the measured OER catalytic activity and the occupancy of the e_g-symmetry electron of the transition metal (M in AMO_3 perovskite). Reprinted by permission from ref. 116 Springer-Nature, Copyright 2011. (B) Linear sweep voltammetry curves and (C) Tafel plot of NiCoS/$Ti_3C_2T_x$ and NiCoS-LDH/$Ti_3C_2T_x$ composites compared to the baseline compound and RuO_2. (D) TOF comparison of the NiCoS/$Ti_3C_2T_x$ composite with RuO_2. (B–D) Reprinted with permission from ref. 117 Copyright 2018 American Chemical Society. (E) Trends in ORR activity of single transition metals plotted as a function of both *O and *OH binding energy. Reprinted with permission from ref. 29 Copyright 2004 American Chemical Society. (F) ORR polarization curves in O_2-saturated 0.1 M KOH showing superior activity of the Fe-phthalocyanine (FePc)/$Ti_3C_2T_x$ hybrid compared to bare FePc and Pt/C benchmark. Reprinted with permission from ref. 120 Copyright 2016 Wiley-VCH Verlag GmbH & Co. KGaA.

the high ORR activity of non-noble metal catalysts in alkaline electrolytes, typically yielding peroxide $(HO_2^-)_{aq}$ that is detectable in the rotating ring disc electrode experiment.

$$*OH + [O_2(H_2O)_n]_{aq} + e^- \rightarrow *OH + (HO_2^{\bullet})_{ads} + OH^- + (H_2O)_{n-1} \quad (26)$$

$$(HO_2^{\bullet})_{ads} + e^- \rightarrow (HO_2^-)_{ads} \quad (27)$$

$$(HO_2^-)_{ads} \rightarrow (HO_2^-)_{aq} \quad (28)$$

While having similar reaction intermediates and electron transfer requirement to OER, ORR (especially in alkaline solution) is more complex with multiple, direct and indirect mechanisms running in parallel. Thus, modelling ORR requires the incorporation of a realistic environment model that includes (explicit) surface water to estimate the charge capacitance of the system.[124] A combination of DFT and kinetic Monte Carlo approaches has uncovered that the ORR activity is significantly affected by the stabilisation of intermediates provided by hydrogen bonds with water molecules from the environment.[125]

Some research has been dedicated to search for a "bifunctional" oxygen catalyst (*i.e.* both OER and ORR active), as it is of great interest to metal–air batteries. However, finding such a material turns out to be challenging, simply because the requirement of variable oxidation states and stable structures at very different working potentials is difficult to fulfill.[104] Perovskites[126] and compounds of Mn that can accommodate multiple stable oxidation

states[127] are the few prominent candidates that demonstrate this bifunctional activity.

As in the case of OER, there are only sparse reports on the use of MXenes as ORR catalysts. Lin *et al.* found that $Ti_3C_2T_x$ only becomes reasonably ORR active (onset potential $\sim$0.8 V *vs.* RHE) after delamination into a single layer with tetrapropylammonium hydroxide.[128] The most striking ORR performance is displayed when MXene is combined with other catalysts with intrinsic ORR activity. Notably, Li *et al.* showed that combining $Ti_3C_2T_x$ with Fe-phthalocyanine (FePc) can result in excellent ORR activity surpassing Pt/C in alkaline electrolytes (Fig. 5F).[120] While FePc is known to be ORR active,[129] combining it with $Ti_3C_2T_x$ doubles its activity. The source of activity enhancement is proposed to be Fe 3d electron delocalisation and spin-state transition of Fe(II) ions upon coupling with $Ti_3C_2T_x$.

In another example, Xue *et al.* prepared $Mn_3O_4/Ti_3C_2T_x$ nanocomposites using the hydrothermal method, and found a dominant four electron transfer ORR mechanism and an onset overpotential as low as that of Pt/C.[130] The enhancement mechanism is fundamentally the same as that for HER and OER as discussed earlier. The Mn_3O_4 nanoparticles were detected to be well dispersed on MXene nanosheets, and they increased the surface area by inhibiting aggregation.[130] Interestingly, the Ti in $Ti_3C_2T_x$ MXene can form strong hybridization with Ag when the alkaline-treated MXene was stirred with $AgNO_3$ solution in the presence of poly(vinylpyrrolidone) and deionized water for 60 mins.[131] The existence of reductive low valence Ti^{2+} and Ti^{3+}, confirmed by XPS, results in the formation of metallic Ag, therefore a hybrid MXene with bimetallic Ag/Ti was obtained. The MXene/$Ag_{0.9}Ti_{0.1}$ nanowire exhibited an onset potential and a half-wave potential of 0.921 and 0.782 V *vs.* RHE at 1600 rpm, respectively, which were significantly more positive than those of the 20 wt% Ag/C catalyst or even pure Ag nanowire.[131] The MXene served not only as a structural support, but also as an efficient charge carrier conductor. The Ti doping induced vacancies or defects also provided more active sites for O_2 adsorption.[131]

While by itself MXene has not been considered as an active ORR catalyst, the synergistic coupling between MXenes and other catalytic materials has opened up a new approach for the development of efficient electrocatalysts. Of particular interest is the fact that MXene coupling can induce a significant change and delocalisation in the catalyst's d-band electronic structure. We note that there is still much to be explored in this area as only one MXene, $Ti_3C_2T_x$, has been investigated. We speculate that, with realisation of new types of MXenes, many interesting properties can be discovered by coupling existing catalyst materials with MXenes.

6. MXene catalysts for CO_2 and N_2 reduction

6.1 CO_2 capture and electrocatalytic CO_2 reduction reaction (CO_2RR)

Electrocatalytic reduction of CO_2 to value-added products has attracted a lot of attention due to its value proposition of creating a closed-loop anthropogenic carbon cycle.[132] Depending on the nature of the catalyst surface, CO_2RR has been proposed to begin with the formation of either *COOH, $*CO_2^-$ radicals or *OCHO.[133–135] From there, a maze of multi-step processes continue towards one or more of the 16 distinct molecular products that have been reported on the Cu surface.[136] With so many viable reaction pathway permutations, finding an excellent catalyst for CO_2RR goes beyond lowering the required overpotential, but also tailoring the catalyst to enhance reaction selectivity towards a certain product. The complexity of CO_2RR has called for advanced DFT approaches beyond computational hydrogen electrode (CHE) models that incorporate explicit solvent layers[44,137] and surface charge.[35]

The "universal" linear dependence of E_a and ΔE on the surface structure of the reaction site proposed by Nørskov and co-workers[83,84] has an overreaching consequence for CO_2RR, especially upon the revelation that the adsorption energies of similarly bound intermediates (*e.g.* *C and *CH; *O and *OH; *etc.*) are linearly correlated.[122,138] These unfavourable scaling relations suggest that the CO_2RR limiting potential is not expected to surpass that of Cu(211),[139] unless a new catalyst surface structure with differently coordinated intermediates is found.

In this regard, MXenes, with delocalized M(1)–M(1) metallic-like bonding states and tuneable surface termination T_x, present a viable solution. Interactions between CO_2 and MXenes have been subjected to theoretical investigations due to their potential use in CO_2 sequestration and activation.[140,141] On bare M_2C MXenes, CO_2 adsorption was found to be relatively strong, with binding strength ranging between -1.13 and -3.69 eV on W_2C and Ti_2C respectively.[140] Like on many transition metal surfaces, the adsorbed CO_2 molecule remains intact but bent, reminding of an activated $CO_2^{\delta-}$ anionic species (on Pt and Ni(111)).[142] It should be noted that DFT calculations performed on bare (non-terminated) MXenes may be unrealistic as most MXenes are quickly functionalized with T_x termination species during synthesis and/or catalytic testing in aqueous solutions.

Li *et al.* screened the interaction between various bare M_3C_2 MXenes (M = group IV, V and VI transition metals) and CO_2 using DFT calculations.[143] Similar to Morales-Garcia *et al.*[140] they found that MXenes can adsorb and activate CO_2, and proceed along the reaction pathway towards CH_4. What's interesting in Li *et al.*'s work is that some of the intermediate molecules appear to be coordinated to the MXene's surface through –O,[143] different from pure transition metal surfaces. Cr_3C_2 and Mo_3C_2 were identified to be the most promising M_3C_2 MXenes for CO_2RR based on the least endergonic overall reaction free energy towards CH_4.

More recently, Handoko *et al.* found that CO_2RR to CH_4 can proceed through a more favourable *HCOOH pathway on the majority of M_2XT_x MXenes.[144] This work takes into account the most favourable terminating species T_x on each M_2XT_x MXene, which is a more accurate representation of actual MXenes. On M_2XT_x MXenes, the intermediates were bound to the MXene surface either through the –C coordination (such as *COOH) or through the –H coordination (such as *HCOOH). Linear scaling relations were established using the binding energies of *COOH

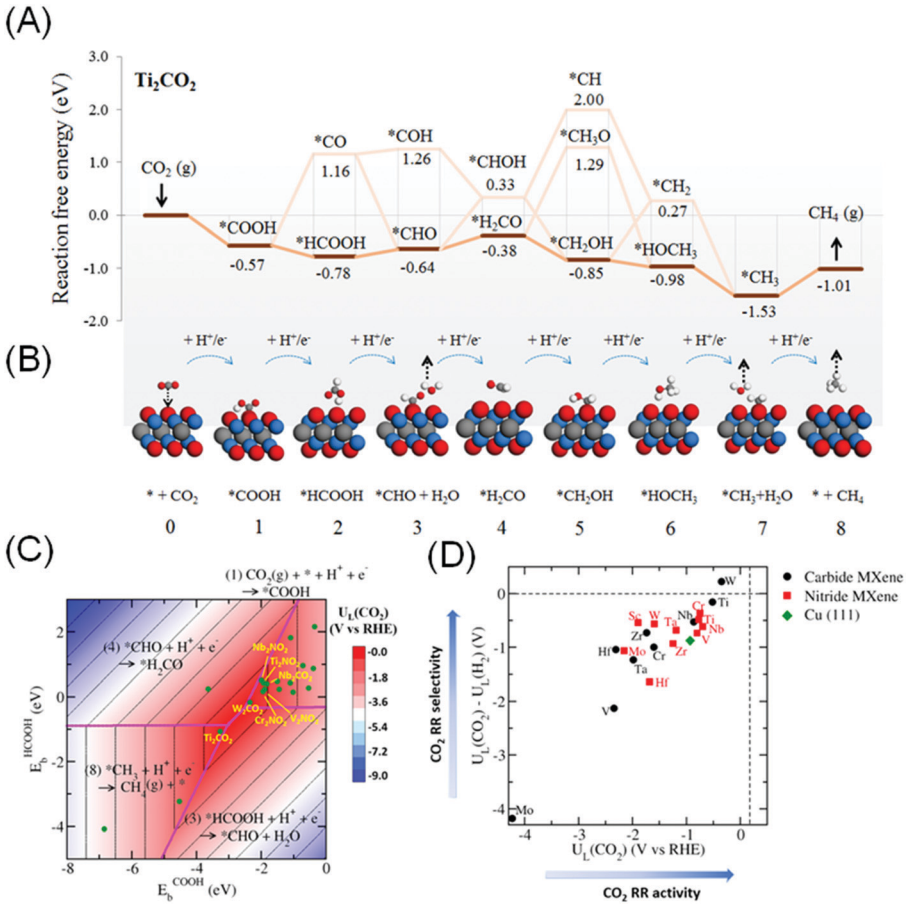

Fig. 6 (A) The lowest energy path and (B) schematics of the molecular adsorption geometry for CO_2RR to CH_4 on Ti_2CO_2 MXene. (C) Contour volcano plot of the limiting potential (U_L) for CO_2RR and (D) plot of $U_L(CO_2)-U_L(H_2)$ against $U_L(CO_2)$, signifying selectivity of the MXene catalyst towards CO_2RR relative to HER. Reprinted from ref. 144 with permission from The Royal Society of Chemistry.

and *HCOOH as important descriptors. Fig. 6A and B depict the reaction coordinate and adsorption configuration on Ti_2CO_2 MXene. W_2CO_2 and Ti_2CO_2 are identified to be promising CO_2RR catalysts, based on the highest CO_2 limiting potential of -0.35 and -0.52 V *vs.* RHE respectively (close to the red apex of the 2D volcano plot shown in Fig. 6C) and best selectivity against competing HER (Fig. 6D). This limiting potential corresponds to the theoretical CO_2RR to CH_4 overpotential of 0.52 and 0.69 V, significantly lower than that of Cu (0.91 to 1.10 V).[145,146]

6.2 Photocatalytic CO_2RR

Research into photocatalytic CO_2RR is largely inspired by the natural photosynthesis process, where complex carbohydrate molecules and oxygen can be obtained from CO_2, water and sunlight.[22] Arguably, photocatalytic CO_2RR is even more challenging than electrocatalytic CO_2RR due to the additional processes of photocarrier generation and charge transfer.[147] These processes are generally inefficient and the quantum yield of photocatalytic CO_2RR is typically less than 1%.[148]

As elaborated previously, most MXenes are not able to generate photocarriers due to their metallic characteristics. Only some –O and –OH terminated MXenes like Ti_2CO_2 and $Sc_2C(OH)_2$ with a narrow bandgap (around 0.9 to 2.0 eV) may be photocatalytically active. DFT calculations suggest that Ti_2CO_2 could be active for photocatalytic CO_2RR to HCOOH.[149] The oxygen vacancy (O_v) on –O terminated Ti_2CO_2 was found to play an essential role in enhancing CO_2 adsorption since the adsorption on a perfect –O terminated surface was too weak. It is interesting that the energy barrier for the rate limiting step was much lower than that of anatase TiO_2.[150]

Instead of being the main photocatalyst, MXenes can also take the role of a co-catalyst or conductive support when combined with an efficient semiconductor photoabsorber during CO_2RR. One of the sources of inefficiency is the relatively poor CO_2 adsorption and activation. Ye *et al.* proposed that the –OH functional groups on the MXene surface may serve as basic sites that facilitate the adsorption of relatively acidic CO_2.[19] The group employed KOH treatment to replace majority –F termination with –OH on $Ti_3C_2T_x$ and combined it as a co-catalyst with the commercial P25 TiO_2 (Fig. 7A). The resulting photocatalytic CO_2RR to CO rate was increased by 3 times and the CH_4 production rate was boosted by 277 times.[19] In another example, a hybrid Ti_3C_2/Bi_2WO_6 composite shows a higher yield of CH_4 and CH_3OH by 4.6 times compared to bare Bi_2WO_6.[151]

Recently Persson *et al.* devised a sequential heating treatment in an H_2 environment during *in situ* TEM experiment to

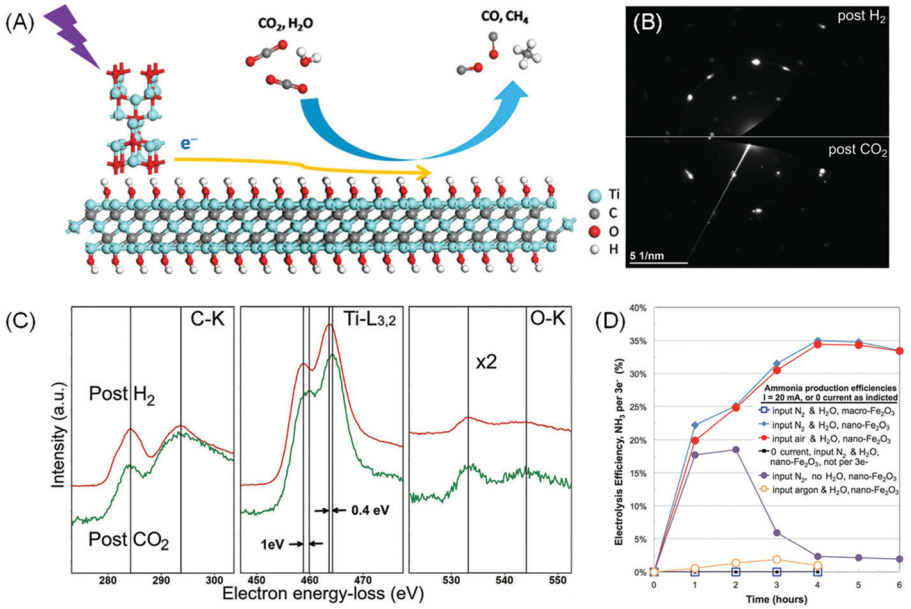

Fig. 7 (A) Proposed photocatalytic CO_2 reduction mechanism on the $Ti_3C_2(OH)_2$/P25 composite under light irradiation. Reprinted with permission from ref. 19 Copyright 2016 Wiley-VCH Verlag GmbH & Co. KGaA. (B) Electron diffraction pattern and (C) EELS spectra on Ti_3C_2 acquired after exposure to 3.5 mbar CO_2 gas at 100 °C for 0.5 h preceded by H_2 exposure for 1 h at 650 °C. From ref. 152 (D) Faradaic efficiency of electrocatalytic N_2 reduction in a molten NaOH/KOH mixture at 200 °C at a constant current of 10 mA cm^{-2}. Different reactions and controls are as described. Reprinted with permission from ref. 153 Copyright 2014 American Association for the Advancement of Science.

realise O-deficient Ti_3C_2 MXene.[152] *In situ* CO_2 exposure to this fresh Ti_3C_2 results in immediate CO_2 saturation on the basal plane while maintaining the 2D structure (Fig. 7B and C). This result shows that careful modification of the MXene surface may also be a viable approach to improve MXene's CO_2 uptake. Introducing MXenes as co-catalysts, with high conductivity, proper band structure alignment (*i.e.* favourable Fermi level) to extract photo-induced electrons, and enhanced active sites for CO_2 adsorption, provides a realistic solution to improve the reaction efficiency. With proper surface engineering, MXenes can be tuned into a semiconductor with a suitable bandgap for photocatalytic CO_2RR.

6.3 N_2 reduction reaction (N_2RR)

Ammonia is an important molecule, widely used for fertilizers, and is an important precursor to most nitrogen containing products, including amines for polymers and basic chemical compounds like nitric acid.[154] Currently, 3–5% of natural gas worldwide is used to make ammonia through successive processes of reverse gas shift, Haber–Bosch and purification, releasing large amounts of CO_2 to the atmosphere.[155] Although the Haber–Bosch process ($N_2 + 3H_2 \rightarrow 2NH_3$) is exothermic, the kinetics are very slow under ambient conditions. These kinetic limitations are overcome by the combination of an iron-based catalyst with high pressure, high temperature conditions.[153]

Electrochemical N_2 reduction ($N_2 + 6H^+ + 6e^- \rightarrow 2NH_3$) aims at forming ammonia under ambient conditions, replacing H_2 as a hydrogen source by proton/electron pairs, therefore reducing the number of process steps, cost and CO_2 emission related to natural gas reforming.[156] Pickett and Talarmin demonstrated the possibility of electrochemically synthesising ammonia from N_2 *via* controlled hydrogenation of a dinitrogen complex (*trans*-$[W(N_2)_2(Ph_2PCH_2CH_2PPh_2)_2]$) over a Hg-pool electrode.[157] While promising, the reaction rate is uncompetitive compared to the high temperature process using H_2. Two approaches are common in electrochemical N_2 reduction: moderate temperature (400–600 °C) using a solid oxide proton conductor electrolyte[158] and an aqueous alkaline electrolyte using a Nafion membrane.[159] Generally the aqueous electrolyte approach is attracting more interest due to higher ammonia TOF, but the overall FE is generally below 1% due to competition from HER. Biological N_2RR using extracted or synthesised Fe-nitrogenases has also been proposed;[160] however, such a process is very sensitive to O_2.

Recently, Licht *et al.* demonstrated that FE up to 35% can be achieved by conducting N_2RR on a dispersed nano-Fe_2O_3 catalyst in molten hydroxide at 200 °C (Fig. 7D).[153] The cell voltage required to drive 10 mA cm^{-2} current density was 1.2 V. However, the proposed contraption was not stable as electrostatics would eventually coagulate the nano-Fe_2O_3 catalyst and halt the electrochemical process.

Herein, MXene has the potential to step into the foray as the state-of-the-art N_2RR catalyst is still based on the same Fe_2O_3 that was used in 1910. Current investigation for MXenes to be applied as N_2RR electrocatalysts is led by theoretical DFT calculations.[161,162] Although N_2 is relatively inert, chemisorption of N_2 on bare M_3C_2 MXenes was found to be spontaneous.[162] Importantly, the N≡N bond appears to be stretched >20% upon adsorption compared to the gas phase, indicating weakening/activation. The first hydrogenation step $*N_2 + *H \rightarrow N\text{–}NH^\bullet$ on V_3C_2 was found to proceed with activation barriers of 0.64 eV,[162] which compares favourably with the 1.98 eV estimated for isolated N_2 to $N_2^{\bullet-}$.[163]

Therefore, MXenes are predicted theoretically to be promising N_2 capture and reduction electrocatalysts. In order to further reduce the energy input, the effect of metal doping in MXenes has been explored, and a low overpotential of 0.47 V was obtained for Fe-doped Mo_2N where Fe-dopants were found to weaken the metal–nitrogen interaction and promote ammonia formation.[161]

7. Future prospects and outlook

7.1 Computations

To date, computational studies of MXenes have been largely dominated by (semi-local) DFT. Since these functionals are notoriously ill adapted for band-gap predictions,[164,165] applications that aim at exploiting the (small) band-gap of T_x terminated MXenes can be especially problematic. In analogy to other 2D materials such as MoS_2[166] or graphitic carbon-nitrides,[167] we encourage the community to rely on the more robust many-body perturbation treatments, also known as the GW approximation. We note that first steps in this direction have already been taken.[168] Furthermore, systematic studies of MXenes' topological electronic structure[169] might reveal particularly intriguing applications.

For the exploitation of MXenes in catalysis, more in-depth studies of the evolution of the surface state as a function of the reactive conditions are needed, *i.e.* reactive gases, ionic species, solvent, electrochemical potential and so on. As in the case of transition metal alloys,[170,171] the surface of MXenes might restructure considerably under reaction conditions, even if the initial or bare surface resembles a randomised alloy. In order to accelerate the development of these catalysts, theoretical insight into the bonding mechanism and the difference compared to transition metal surfaces can be obtained *via* energy decomposition analysis, recently extended to metallic surfaces.[172]

To obtain an atomistic understanding of the working catalyst and promising performance of MXenes in electrocatalysis, efforts towards the inclusion of the electrochemical potential and the influence of the solvent need to be made.[36,37,46,173,174] These efforts are not specific to MXenes, but generally necessary for metallic catalysts. Both aspects are highly challenging and not always fully separable; to account for the electrochemical potential, the electrolyte also needs to be modelled. On the other hand, in the context of bio-mass valorization,[175] aqueous solution-based catalytic processes over metal catalysts are on the rise.[176] In these processes, the chemisorption of water molecules at the solid/liquid interface has been shown to significantly modify the reactivity of the catalyst.[177] Although highly challenging to model even for mildly reactive surfaces such as Pt(111),[178] the structuration of the metal/liquid interface is expected to depend on the nature of the MXenes and their surface termination, which may open the door to more active and selective catalysts compared to known transition metal based nanostructures.

7.2 Applications

As an important family of post-graphene 2D materials, MXenes have made a significant impact on sustainable energy storage and conversion. But most of the research on MXenes for electro- and photocatalysis is still at its early stage. Although theoretical calculations predict that MXenes can be promising efficient catalysts for many energy conversion reactions, their experimental investigation is still limited to a few compositions, and their roles in OER, ORR, CO_2RR and N_2RR are still waiting to be further explored. We could expect remarkable performances for other MXene compositions, *e.g.* nitride-based MXenes are predicted to exhibit better CO_2 adsorption than their carbide analogues.

Besides acting as an individual electrocatalyst, MXenes found their important role by coupling with other materials to form hybrid catalysts for HER, OER, ORR, CO_2RR and N_2RR, though most of the investigations were based on $Ti_3C_2T_x$ MXene. Since there are 22 different MXenes reported until now, the exploration of other compositions and their coupling effects with various existing catalysts could certainly bring many interesting results. We expect that the coupling of the unique properties of MXenes with other CO_2RR catalysts such as Cu and careful composition and structural engineering, will boost the reaction activity and selectivity. Similar to the synergistic effects observed in electrocatalysis, we also expect new combinations of MXenes and other semiconducting materials to significantly improve photocatalysis reactions. Overall, MXenes as catalysts or co-catalysts are still a relatively under-explored field, and theory-guided materials design is expected to bring about significant breakthroughs in clean energy research in the near future.

Conflicts of interest

There are no conflicts of interest to declare.

Acknowledgements

This work was supported by the Institute of Materials Research and Engineering, A*STAR (IMRE/17-1R1211).

References

1 *Monthly Energy Review July 2018*, U.S. Energy Information Administration, 2018.
2 M. Höök and X. Tang, *Energy Policy*, 2013, **52**, 797–809.
3 Z. W. Seh, J. Kibsgaard, C. F. Dickens, I. Chorkendorff, J. K. Nørskov and T. F. Jaramillo, *Science*, 2017, **355**, eaad4998.
4 B. Anasori, M. R. Lukatskaya and Y. Gogotsi, *Nat. Rev. Mater.*, 2017, **2**, 16098.
5 M. Naguib, M. Kurtoglu, V. Presser, J. Lu, J. Niu, M. Heon, L. Hultman, Y. Gogotsi and M. W. Barsoum, *Adv. Mater.*, 2011, **23**, 4248–4253.
6 M. Alhabeb, K. Maleski, B. Anasori, P. Lelyukh, L. Clark, S. Sin and Y. Gogotsi, *Chem. Mater.*, 2017, **29**, 7633–7644.
7 B. Soundiraraju and B. K. George, *ACS Nano*, 2017, **11**, 8892–8900.
8 P. Urbankowski, B. Anasori, K. Hantanasirisakul, L. Yang, L. Zhang, B. Haines, S. J. May, S. J. L. Billinge and Y. Gogotsi, *Nanoscale*, 2017, **9**, 17722–17730.

9 Y. Huang, A. D. Handoko, P. Hirunsit and B. S. Yeo, *ACS Catal.*, 2017, **7**, 1749–1756.
10 A. D. Handoko, K. D. Fredrickson, B. Anasori, K. W. Convey, L. R. Johnson, Y. Gogotsi, A. Vojvodic and Z. W. Seh, *ACS Appl. Energy Mater.*, 2018, **1**, 173–180.
11 J. Di, C. Yan, A. D. Handoko, Z. W. Seh, H. Li and Z. Liu, *Mater. Today*, 2018, **21**, 749–770.
12 A. D. Handoko, C. W. Ong, Y. Huang, Z. G. Lee, L. Lin, G. B. Panetti and B. S. Yeo, *J. Phys. Chem. C*, 2016, **120**, 20058–20067.
13 R. Reske, H. Mistry, F. Behafarid, B. Roldan Cuenya and P. Strasser, *J. Am. Chem. Soc.*, 2014, **136**, 6978–6986.
14 H. Xiao, W. A. Goddard, T. Cheng and Y. Liu, *Proc. Natl. Acad. Sci. U. S. A.*, 2017, **114**, 6685–6688.
15 J. Zhang, Y. Zhao, X. Guo, C. Chen, C.-L. Dong, R.-S. Liu, C.-P. Han, Y. Li, Y. Gogotsi and G. Wang, *Nat. Catal.*, 2018, **1**, 985–992.
16 S. Zhou, X. Yang, W. Pei, N. Liu and J. Zhao, *Nanoscale*, 2018, **10**, 10876–10883.
17 H. Wang, R. Peng, Z. D. Hood, M. Naguib, S. P. Adhikari and Z. Wu, *ChemSusChem*, 2016, **9**, 1490–1497.
18 J. Ran, G. Gao, F.-T. Li, T.-Y. Ma, A. Du and S.-Z. Qiao, *Nat. Commun.*, 2017, **8**, 13907.
19 M. Ye, X. Wang, E. Liu, J. Ye and D. Wang, *ChemSusChem*, 2018, **11**, 1606–1611.
20 S. Ho-Kimura, S. J. A. Moniz, A. D. Handoko and J. Tang, *J. Mater. Chem. A*, 2014, **2**, 3948–3953.
21 E. Pastor, F. M. Pesci, A. Reynal, A. D. Handoko, M. Guo, X. An, A. J. Cowan, D. Klug, J. Durrant and J. Tang, *Phys. Chem. Chem. Phys.*, 2014, **16**, 5922–5926.
22 Y. Tachibana, L. Vayssieres and J. R. Durrant, *Nat. Photonics*, 2012, **6**, 511–518.
23 A. J. Cowan, J. Tang, W. Leng, J. R. Durrant and D. R. Klug, *J. Phys. Chem. C*, 2010, **114**, 4208–4214.
24 A. D. Handoko, F. Wei, Jenndy, B. S. Yeo and Z. W. Seh, *Nat. Catal.*, 2018, **1**, 922–934.
25 S. Fletcher, *J. Solid State Electrochem.*, 2009, **13**, 537–549.
26 P. Sabatier, *La catalyse en chimie organique*, C. Béranger, Paris, 1913.
27 P. Trens, R. Durand, B. Coq, C. Coutanceau, S. Rousseau and C. Lamy, *Appl. Catal., B*, 2009, **92**, 280–284.
28 R. Parsons, in *Synchrotron Techniques in Interfacial Electrochemistry*, ed. C. A. Melendres and A. Tadjeddine, Springer, Netherlands, Dordrecht, 1994, pp. 21–32.
29 J. K. Nørskov, J. Rossmeisl, A. Logadottir, L. Lindqvist, J. R. Kitchin, T. Bligaard and H. Jónsson, *J. Phys. Chem. B*, 2004, **108**, 17886–17892.
30 J. K. Nørskov, T. Bligaard, B. Hvolbæk, F. Abild-Pedersen, I. Chorkendorff and C. H. Christensen, *Chem. Soc. Rev.*, 2008, **37**, 2163–2171.
31 J. Suntivich, K. J. May, H. A. Gasteiger, J. B. Goodenough and Y. Shao-Horn, *Science*, 2011, **334**, 1383–1385.
32 V. Viswanathan, H. A. Hansen, J. Rossmeisl and J. K. Nørskov, *ACS Catal.*, 2012, **2**, 1654–1660.
33 I. C. Man, H.-Y. Su, F. Calle-Vallejo, H. A. Hansen, J. I. Martínez, N. G. Inoglu, J. Kitchin, T. F. Jaramillo, J. K. Nørskov and J. Rossmeisl, *ChemCatChem*, 2011, **3**, 1159–1165.
34 V. R. Stamenkovic, B. S. Mun, M. Arenz, K. J. J. Mayrhofer, C. A. Lucas, G. Wang, P. N. Ross and N. M. Markovic, *Nat. Mater.*, 2007, **6**, 241.
35 S. N. Steinmann, C. Michel, R. Schwiedernoch, J.-S. Filhol and P. Sautet, *ChemPhysChem*, 2015, **16**, 2307–2311.
36 J. D. Goodpaster, A. T. Bell and M. Head-Gordon, *J. Phys. Chem. Lett.*, 2016, **7**, 1471–1477.
37 T. Cheng, L. Wang, B. V. Merinov and W. A. Goddard, *J. Am. Chem. Soc.*, 2018, **140**, 7787–7790.
38 K. S. Exner and H. Over, *Acc. Chem. Res.*, 2017, **50**, 1240–1247.
39 K. S. Exner, I. Sohrabnejad-Eskan, J. Anton, T. Jacob and H. Over, *ChemElectroChem*, 2017, **4**, 2902–2908.
40 K. Chan and J. K. Nørskov, *J. Phys. Chem. Lett.*, 2016, **7**, 1686–1690.
41 X. Nie, M. R. Esopi, M. J. Janik and A. Asthagiri, *Angew. Chem.*, 2013, **125**, 2519–2522.
42 Y.-H. Fang and Z.-P. Liu, *J. Am. Chem. Soc.*, 2010, **132**, 18214–18222.
43 K. Letchworth-Weaver and T. A. Arias, *Phys. Rev. B*, 2012, **86**, 075140.
44 S. N. Steinmann, C. Michel, R. Schwiedernoch and P. Sautet, *Phys. Chem. Chem. Phys.*, 2015, **17**, 13949–13963.
45 B. Schweitzer, S. N. Steinmann and C. Michel, *Phys. Chem. Chem. Phys.*, 2019, **21**, 5368–5377.
46 C. D. Taylor, S. A. Wasileski, J.-S. Filhol and M. Neurock, *Phys. Rev. B*, 2006, **73**, 165402.
47 J. Hussain, H. Jónsson and E. Skúlason, *ACS Catal.*, 2018, **8**, 5240–5249.
48 M. Khazaei, A. Ranjbar, M. Arai, T. Sasaki and S. Yunoki, *J. Mater. Chem. C*, 2017, **5**, 2488–2503.
49 I. R. Shein and A. L. Ivanovskii, *Comput. Mater. Sci.*, 2012, **65**, 104–114.
50 M. Naguib, R. R. Unocic, B. L. Armstrong and J. Nanda, *Dalton Trans.*, 2015, **44**, 9353–9358.
51 O. Mashtalir, M. R. Lukatskaya, M. Q. Zhao, M. W. Barsoum and Y. Gogotsi, *Adv. Mater.*, 2015, **27**, 3501–3506.
52 D. Geng, X. Zhao, Z. Chen, W. Sun, W. Fu, J. Chen, W. Liu, W. Zhou and K. P. Loh, *Adv. Mater.*, 2017, **29**, 1700072.
53 D. Geng, X. Zhao, L. Li, P. Song, B. Tian, W. Liu, J. Chen, D. Shi, M. Lin, W. Zhou and K. P. Loh, *2D Mater.*, 2017, **4**, 011012.
54 B. Wang, A. Zhou, Q. Hu and L. Wang, *Int. J. Appl. Ceram. Technol.*, 2017, **14**, 873–879.
55 C. Cui, M. Hu, C. Zhang, R. Cheng, J. Yang and X. Wang, *Chem. Commun.*, 2018, **54**, 8132–8135.
56 P. Urbankowski, B. Anasori, T. Makaryan, D. Er, S. Kota, P. L. Walsh, M. Zhao, V. B. Shenoy, M. W. Barsoum and Y. Gogotsi, *Nanoscale*, 2016, **8**, 11385–11391.
57 J. Zhou, X. Zha, F. Y. Chen, Q. Ye, P. Eklund, S. Du and Q. Huang, *Angew. Chem., Int. Ed.*, 2016, **55**, 5008–5013.
58 M. Naguib, V. N. Mochalin, M. W. Barsoum and Y. Gogotsi, *Adv. Mater.*, 2014, **26**, 992–1005.
59 M. Naguib, O. Mashtalir, J. Carle, V. Presser, J. Lu, L. Hultman, Y. Gogotsi and M. W. Barsoum, *ACS Nano*, 2012, **6**, 1322–1331.
60 M. A. Hope, A. C. Forse, K. J. Griffith, M. R. Lukatskaya, M. Ghidiu, Y. Gogotsi and C. P. Grey, *Phys. Chem. Chem. Phys.*, 2016, **18**, 5099–5102.

61 T. Hu, Z. Li, M. Hu, J. Wang, Q. Hu, Q. Li and X. Wang, *J. Phys. Chem. C*, 2017, **121**, 19254–19261.
62 A. Champagne, L. Shi, T. Ouisse, B. Hackens and J.-C. Charlier, *Phys. Rev. B*, 2018, **97**, 115439.
63 X.-H. Zha, K. Luo, Q. Li, Q. Huang, J. He, X. Wen and S. Du, *EPL*, 2015, **111**, 26007.
64 Y. Xie, M. Naguib, V. N. Mochalin, M. W. Barsoum, Y. Gogotsi, X. Yu, K. W. Nam, X. Q. Yang, A. I. Kolesnikov and P. R. Kent, *J. Am. Chem. Soc.*, 2014, **136**, 6385–6394.
65 Q. Tang, Z. Zhou and P. Shen, *J. Am. Chem. Soc.*, 2012, **134**, 16909–16916.
66 Q. Peng, J. Guo, Q. Zhang, J. Xiang, B. Liu, A. Zhou, R. Liu and Y. Tian, *J. Am. Chem. Soc.*, 2014, **136**, 4113–4116.
67 C. Si, J. Zhou and Z. Sun, *ACS Appl. Mater. Interfaces*, 2015, **7**, 17510–17515.
68 M. Khazaei, M. Arai, T. Sasaki, C.-Y. Chung, N. S. Venkataramanan, M. Estili, Y. Sakka and Y. Kawazoe, *Adv. Funct. Mater.*, 2013, **23**, 2185–2192.
69 N. Zhang, Y. Hong, S. Yazdanparast and M. A. Zaeem, *2D Mater.*, 2018, **5**, 045004.
70 G. R. Berdiyorov, *EPL*, 2015, **111**, 67002.
71 P. Li, J. Zhu, A. D. Handoko, R. Zhang, H. Wang, D. Legut, X. Wen, Z. Fu, Z. W. Seh and Q. Zhang, *J. Mater. Chem. A*, 2018, **6**, 4271–4278.
72 B. Anasori, J. Halim, J. Lu, C. A. Voigt, L. Hultman and M. W. Barsoum, *Scr. Mater.*, 2015, **101**, 5–7.
73 J. Yang, M. Naguib, M. Ghidiu, L.-M. Pan, J. Gu, J. Nanda, J. Halim, Y. Gogotsi and M. W. Barsoum, *J. Am. Ceram. Soc.*, 2016, **99**, 660–666.
74 B. Anasori, Y. Xie, M. Beidaghi, J. Lu, B. C. Hosler, L. Hultman, P. R. C. Kent, Y. Gogotsi and M. W. Barsoum, *ACS Nano*, 2015, **9**, 9507–9516.
75 W. Sun, Y. Xie and P. R. C. Kent, *Nanoscale*, 2018, **10**, 11962–11968.
76 L. Dong, H. Kumar, B. Anasori, Y. Gogotsi and V. B. Shenoy, *J. Phys. Chem. Lett.*, 2017, **8**, 422–428.
77 M. Khazaei, A. Ranjbar, M. Arai and S. Yunoki, *Phys. Rev. B*, 2016, **94**, 125152.
78 V. N. Borysiuk, V. N. Mochalin and Y. Gogotsi, *Nanotechnology*, 2015, **26**, 265705.
79 G. Gao, A. P. O'Mullane and A. Du, *ACS Catal.*, 2017, **7**, 494–500.
80 M. Pandey and K. S. Thygesen, *J. Phys. Chem. C*, 2017, **121**, 13593–13598.
81 F. Shahzad, M. Alhabeb, C. B. Hatter, B. Anasori, S. Man Hong, C. M. Koo and Y. Gogotsi, *Science*, 2016, **353**, 1137–1140.
82 H. Wang, Y. Wu, J. Zhang, G. Li, H. Huang, X. Zhang and Q. Jiang, *Mater. Lett.*, 2015, **160**, 537–540.
83 J. K. Nørskov, T. Bligaard, A. Logadottir, S. Bahn, L. B. Hansen, M. Bollinger, H. Bengaard, B. Hammer, Z. Sljivancanin, M. Mavrikakis, Y. Xu, S. Dahl and C. J. H. Jacobsen, *J. Catal.*, 2002, **209**, 275–278.
84 T. Bligaard, J. K. Nørskov, S. Dahl, J. Matthiesen, C. H. Christensen and J. Sehested, *J. Catal.*, 2004, **224**, 206–217.
85 F. Calle-Vallejo, J. Tymoczko, V. Colic, Q. H. Vu, M. D. Pohl, K. Morgenstern, D. Loffreda, P. Sautet, W. Schuhmann and A. S. Bandarenka, *Science*, 2015, **350**, 185–189.
86 T. F. Jaramillo, K. P. Jørgensen, J. Bonde, J. H. Nielsen, S. Horch and I. Chorkendorff, *Science*, 2007, **317**, 100–102.
87 Z. W. Seh, K. D. Fredrickson, B. Anasori, J. Kibsgaard, A. L. Strickler, M. R. Lukatskaya, Y. Gogotsi, T. F. Jaramillo and A. Vojvodic, *ACS Energy Lett.*, 2016, **1**, 589–594.
88 C. Ling, L. Shi, Y. Ouyang and J. Wang, *Chem. Mater.*, 2016, **28**, 9026–9032.
89 Y. Yu, S.-Y. Huang, Y. Li, S. N. Steinmann, W. Yang and L. Cao, *Nano Lett.*, 2014, **14**, 553–558.
90 S. Li, P. Tuo, J. Xie, X. Zhang, J. Xu, J. Bao, B. Pan and Y. Xie, *Nano Energy*, 2018, **47**, 512–518.
91 W. Yuan, L. Cheng, Y. An, H. Wu, N. Yao, X. Fan and X. Guo, *ACS Sustainable Chem. Eng.*, 2018, **6**, 8976–8982.
92 X. Wu, Z. Wang, M. Yu, L. Xiu and J. Qiu, *Adv. Mater.*, 2017, **29**, 1607017.
93 Y. Liu, H. Xiao and W. A. Goddard, *J. Am. Chem. Soc.*, 2016, **138**, 15853–15856.
94 J. You, C. Si, J. Zhou and Z. Sun, *J. Phys. Chem. C*, 2019, **123**, 3719–3726.
95 C. Ling, L. Shi, Y. Ouyang, Q. Chen and J. Wang, *Adv. Sci.*, 2016, **3**, 1600180.
96 R. Meshkian, M. Dahlqvist, J. Lu, B. Wickman, J. Halim, J. Thörnberg, Q. Tao, S. Li, S. Intikhab, J. Snyder, M. W. Barsoum, M. Yildizhan, J. Palisaitis, L. Hultman, P. O. Å. Persson and J. Rosen, *Adv. Mater.*, 2018, **30**, 1706409.
97 M. Mavrikakis, B. Hammer and J. K. Nørskov, *Phys. Rev. Lett.*, 1998, **81**, 2819–2822.
98 P. Strasser, S. Koh, T. Anniyev, J. Greeley, K. More, C. Yu, Z. Liu, S. Kaya, D. Nordlund, H. Ogasawara, M. F. Toney and A. Nilsson, *Nat. Chem.*, 2010, **2**, 454–460.
99 G. Gao, G. Ding, J. Li, K. Yao, M. Wu and M. Qian, *Nanoscale*, 2016, **8**, 8986–8994.
100 M. Shao, Y. Shao, J. Chai, Y. Qu, M. Yang, Z. Wang, M. Yang, W. F. Ip, C. T. Kwok, X. Shi, Z. Lu, S. Wang, X. Wang and H. Pan, *J. Mater. Chem. A*, 2017, **5**, 16748–16756.
101 Y. Sun, D. Jin, Y. Sun, X. Meng, Y. Gao, Y. Dall'Agnese, G. Chen and X.-F. Wang, *J. Mater. Chem. A*, 2018, **6**, 9124–9131.
102 A. C. Rajan, A. Mishra, S. Satsangi, R. Vaish, H. Mizuseki, K.-R. Lee and A. K. Singh, *Chem. Mater.*, 2018, **30**, 4031–4038.
103 K. Xiong, P. Wang, G. Yang, Z. Liu, H. Zhang, S. Jin and X. Xu, *Sci. Rep.*, 2017, **7**, 15095.
104 Y. Li and H. Dai, *Chem. Soc. Rev.*, 2014, **43**, 5257–5275.
105 Y. Matsumoto and E. Sato, *Mater. Chem. Phys.*, 1986, **14**, 397–426.
106 H. Dau, L. Iuzzolino and J. Dittmer, *Biochim. Biophys. Acta*, 2001, **1503**, 24–39.
107 A. D. Handoko, S. Deng, Y. Deng, A. W. F. Cheng, K. W. Chan, H. R. Tan, Y. Pan, E. S. Tok, C. H. Sow and B. S. Yeo, *Catal. Sci. Technol.*, 2016, **6**, 269–274.
108 Y. Deng, A. D. Handoko, Y. Du, S. Xi and B. S. Yeo, *ACS Catal.*, 2016, **6**, 2473–2481.
109 J. O. M. Bockris, *J. Chem. Phys.*, 1956, **24**, 817–827.
110 J. O. Bockris and T. Otagawa, *J. Phys. Chem.*, 1983, **87**, 2960–2971.
111 R. L. Doyle and M. E. G. Lyons, in *Photoelectrochemical Solar Fuel Production: From Basic Principles to Advanced*

Devices, ed. S. Giménez and J. Bisquert, Springer International Publishing, Cham, 2016, pp. 41–104.
112 C.-H. Lee, A. Riga and E. Yeager, in *Mass Transport Phenomena in Ceramics*, ed. A. R. Cooper and A. H. Heuer, Springer US, Boston, MA, 1975, pp. 489–499.
113 Y. Surendranath, M. W. Kanan and D. G. Nocera, *J. Am. Chem. Soc.*, 2010, **132**, 16501–16509.
114 S. Trasatti, *J. Electroanal. Chem. Interfacial Electrochem.*, 1980, **111**, 125–131.
115 J. Rossmeisl, Z. W. Qu, H. Zhu, G. J. Kroes and J. K. Nørskov, *J. Electroanal. Chem.*, 2007, **607**, 83–89.
116 J. Suntivich, H. A. Gasteiger, N. Yabuuchi, H. Nakanishi, J. B. Goodenough and Y. Shao-Horn, *Nat. Chem.*, 2011, **3**, 546–550.
117 H. Zou, B. He, P. Kuang, J. Yu and K. Fan, *ACS Appl. Mater. Interfaces*, 2018, **10**, 22311–22319.
118 M. Yu, S. Zhou, Z. Wang, J. Zhao and J. Qiu, *Nano Energy*, 2018, **44**, 181–190.
119 T. Y. Ma, J. L. Cao, M. Jaroniec and S. Z. Qiao, *Angew. Chem., Int. Ed.*, 2016, **55**, 1138–1142.
120 Z. Li, Z. Zhuang, F. Lv, H. Zhu, L. Zhou, M. Luo, J. Zhu, Z. Lang, S. Feng, W. Chen, L. Mai and S. Guo, *Adv. Mater.*, 2018, **30**, 1803220.
121 J. K. Nørskov, T. Bligaard, A. Logadottir, J. R. Kitchin, J. G. Chen, S. Pandelov and U. Stimming, *J. Electrochem. Soc.*, 2005, **152**, J23–J26.
122 F. Abild-Pedersen, J. Greeley, F. Studt, J. Rossmeisl, T. Munter, P. Moses, E. Skúlason, T. Bligaard and J. Nørskov, *Phys. Rev. Lett.*, 2007, **99**, 016105.
123 N. Ramaswamy and S. Mukerjee, *J. Phys. Chem. C*, 2011, **115**, 18015–18026.
124 J. Rossmeisl, J. K. Nørskov, C. D. Taylor, M. J. Janik and M. Neurock, *J. Phys. Chem. B*, 2006, **110**, 21833–21839.
125 S. Liu, M. G. White and P. Liu, *J. Phys. Chem. C*, 2016, **120**, 15288–15298.
126 J.-I. Jung, M. Risch, S. Park, M. G. Kim, G. Nam, H.-Y. Jeong, Y. Shao-Horn and J. Cho, *Energy Environ. Sci.*, 2016, **9**, 176–183.
127 G. Fu, X. Jiang, Y. Chen, L. Xu, D. Sun, J.-M. Lee and Y. Tang, *NPG Asia Mater.*, 2018, **10**, 618–629.
128 H. Lin, L. Chen, X. Lu, H. Yao, Y. Chen and J. Shi, *Sci. China Mater.*, 2018, **62**, 662–670.
129 W. Li, A. Yu, D. C. Higgins, B. G. Llanos and Z. Chen, *J. Am. Chem. Soc.*, 2010, **132**, 17056–17058.
130 Q. Xue, Z. Pei, Y. Huang, M. Zhu, Z. Tang, H. Li, Y. Huang, N. Li, H. Zhang and C. Zhi, *J. Mater. Chem. A*, 2017, **5**, 20818–20823.
131 Z. Zhang, H. Li, G. Zou, C. Fernandez, B. Liu, Q. Zhang, J. Hu and Q. Peng, *ACS Sustainable Chem. Eng.*, 2016, **4**, 6763–6771.
132 G. A. Olah, G. K. Prakash and A. Goeppert, *J. Am. Chem. Soc.*, 2011, **133**, 12881–12898.
133 B. A. Rosen, A. Salehi-Khojin, M. R. Thorson, W. Zhu, D. T. Whipple, P. J. A. Kenis and R. I. Masel, *Science*, 2011, **334**, 643–644.
134 R. Kortlever, J. Shen, K. J. P. Schouten, F. Calle-Vallejo and M. T. M. Koper, *J. Phys. Chem. Lett.*, 2015, **6**, 4073–4082.
135 J. T. Feaster, C. Shi, E. R. Cave, T. Hatsukade, D. N. Abram, K. P. Kuhl, C. Hahn, J. K. Nørskov and T. F. Jaramillo, *ACS Catal.*, 2017, **7**, 4822–4827.
136 K. P. Kuhl, T. Hatsukade, E. R. Cave, D. N. Abram, J. Kibsgaard and T. F. Jaramillo, *J. Am. Chem. Soc.*, 2014, **136**, 14107–14113.
137 T. Cheng, H. Xiao and W. A. Goddard, *Proc. Natl. Acad. Sci. U. S. A.*, 2017, **114**, 1795–1800.
138 F. Calle-Vallejo, J. Martínez, J. García-Lastra, J. Rossmeisl and M. Koper, *Phys. Rev. Lett.*, 2012, **108**, 116103.
139 C. Shi, H. A. Hansen, A. C. Lausche and J. K. Norskov, *Phys. Chem. Chem. Phys.*, 2014, **16**, 4720–4727.
140 Á. Morales-García, A. Fernández-Fernández, F. Viñes and F. Illas, *J. Mater. Chem. A*, 2018, **6**, 3381–3385.
141 R. Morales-Salvador, Á. Morales-García, F. Viñes and F. Illas, *Phys. Chem. Chem. Phys.*, 2018, **20**, 17117–17124.
142 S. N. Steinmann, C. Michel, R. Schwiedernoch, M. Wu and P. Sautet, *J. Catal.*, 2016, **343**, 240–247.
143 N. Li, X. Chen, W.-J. Ong, D. R. MacFarlane, X. Zhao, A. K. Cheetham and C. Sun, *ACS Nano*, 2017, **11**, 10825–10833.
144 A. D. Handoko, K. H. Khoo, T. L. Tan, H. Jin and Z. W. Seh, *J. Mater. Chem. A*, 2018, **6**, 21885–21890.
145 A. A. Peterson, F. Abild-Pedersen, F. Studt, J. Rossmeisl and J. K. Norskov, *Energy Environ. Sci.*, 2010, **3**, 1311–1315.
146 X. Hong, K. Chan, C. Tsai and J. K. Nørskov, *ACS Catal.*, 2016, **6**, 4428–4437.
147 A. D. Handoko, K. Li and J. Tang, *Curr. Opin. Chem. Eng.*, 2013, **2**, 200–206.
148 G. Sahara and O. Ishitani, *Inorg. Chem.*, 2015, **54**, 5096–5104.
149 X. Zhang, Z. Zhang, J. Li, X. Zhao, D. Wu and Z. Zhou, *J. Mater. Chem. A*, 2017, **5**, 12899–12903.
150 Y. Ji and Y. Luo, *ACS Catal.*, 2016, **6**, 2018–2025.
151 S. Cao, B. Shen, T. Tong, J. Fu and J. Yu, *Adv. Funct. Mater.*, 2018, **28**, 1800136.
152 I. Persson, J. Halim, H. Lind, T. W. Hansen, J. B. Wagner, L.-Å. Näslund, V. Darakchieva, J. Palisaitis, J. Rosen and P. O. Å. Persson, *Adv. Mater.*, 2019, **31**, 1805472.
153 S. Licht, B. Cui, B. Wang, F.-F. Li, J. Lau and S. Liu, *Science*, 2014, **345**, 637–640.
154 L. Lassaletta, G. Billen, B. Grizzetti, J. Anglade and J. Garnier, *Environ. Res. Lett.*, 2014, **9**, 105011.
155 V. Smil, *Enriching the Earth: Fritz Haber, Carl Bosch, and the Transformation of World Food Production*, MIT Press, Cambridge, 2004.
156 I. A. Amar, R. Lan, C. T. G. Petit and S. Tao, *J. Solid State Electrochem.*, 2011, **15**, 1845.
157 C. J. Pickett and J. Talarmin, *Nature*, 1985, **317**, 652–653.
158 F. Kosaka, T. Nakamura, A. Oikawa and J. Otomo, *ACS Sustainable Chem. Eng.*, 2017, **5**, 10439–10446.
159 R. Lan, J. T. S. Irvine and S. Tao, *Sci. Rep.*, 2013, **3**, 1145.
160 D. F. Harris, D. A. Lukoyanov, S. Shaw, P. Compton, M. Tokmina-Lukaszewska, B. Bothner, N. Kelleher, D. R. Dean, B. M. Hoffman and L. C. Seefeldt, *Biochemistry*, 2018, **57**, 701–710.
161 Q. Li, L. He, C. Sun and X. Zhang, *J. Phys. Chem. C*, 2017, **121**, 27563–27568.
162 L. M. Azofra, N. Li, D. R. MacFarlane and C. Sun, *Energy Environ. Sci.*, 2016, **9**, 2545–2549.

163 J. S. Anderson, J. Rittle and J. C. Peters, *Nature*, 2013, **501**, 84.
164 H. Xiao, J. Tahir-Kheli and W. A. Goddard, *J. Phys. Chem. Lett.*, 2011, **2**, 212–217.
165 T. Le Bahers, M. Rérat and P. Sautet, *J. Phys. Chem. C*, 2014, **118**, 5997–6008.
166 D. Y. Qiu, F. H. da Jornada and S. G. Louie, *Phys. Rev. B*, 2016, **93**, 235435.
167 S. N. Steinmann, S. T. A. G. Melissen, T. Le Bahers and P. Sautet, *J. Mater. Chem. A*, 2017, **5**, 5115–5122.
168 Y. Zhang, W. Xia, Y. Wu and P. Zhang, *Nanoscale*, 2019, **11**, 3993–4000.
169 B. Bradlyn, L. Elcoro, J. Cano, M. G. Vergniory, Z. Wang, C. Felser, M. I. Aroyo and B. A. Bernevig, *Nature*, 2017, **547**, 298.
170 E. Vignola, S. N. Steinmann, K. Le Mapihan, B. D. Vandegehuchte, D. Curulla and P. Sautet, *J. Phys. Chem. C*, 2018, **122**, 15456–15463.
171 F. Tao and M. Salmeron, *Science*, 2011, **331**, 171–174.
172 R. Staub, M. Iannuzzi, R. Z. Khaliullin and S. N. Steinmann, *J. Chem. Theory Comput.*, 2019, **15**, 265–275.
173 S. N. Steinmann and P. Sautet, *J. Phys. Chem. C*, 2016, **120**, 5619–5623.
174 R. Sundararaman, W. A. GoddardIII and T. A. Arias, *J. Chem. Phys.*, 2017, **146**, 114104.
175 R. A. Sheldon, *Green Chem.*, 2014, **16**, 950–963.
176 R. Réocreux and C. Michel, *Curr. Opin. Green Sustain. Chem.*, 2018, **10**, 51–59.
177 C. Michel, J. Zaffran, A. M. Ruppert, J. Matras-Michalska, M. Jędrzejczyk, J. Grams and P. Sautet, *Chem. Commun.*, 2014, **50**, 12450–12453.
178 S. N. Steinmann, R. Ferreira De Morais, A. W. Götz, P. Fleurat-Lessard, M. Iannuzzi, P. Sautet and C. Michel, *J. Chem. Theory Comput.*, 2018, **14**, 3238–3251.